DEVELOPMENT OF A REAL-TIME INSTRUMENT TO
MEASURE ENTRANCE SKIN EXPOSURE FREE-IN-AIR
DURING RADIOGRAPHIC AND FLUOROSCOPIC EXAMINATIONS

BY

STEVEN JAY KNAPP

A DISSERTATION PRESENTED TO THE GRADUATE SCHOOL
OF THE UNIVERSITY OF FLORIDA IN PARTIAL FULFILLMENT
OF THE REQUIREMENTS FOR THE DEGREE OF
DOCTOR OF PHILOSOPHY

UNIVERSITY OF FLORIDA

1996

TABLE OF CONTENTS

iv

LIST OF TABLES

LIST OF FIGURES

DEVELOPMENT OF A REAL-TIME INSTRUMENT TO
MEASURE ENTRANCE SKIN EXPOSURE FREE-IN-AIR
DURING RADIOGRAPHIC AND FLUOROSCOPIC EXAMINATIONS

By

Steven Jay Knapp

May, 1996

In order to obtain the information necessary for an
actual dose assessment for a patient, the medical physicist
generally requires determination of the entrance skin
exposure (free-in-air) ESE. ESE is the measured exposure
without backscatter at the entrance plane of a patient's
skin. Once the measurement of ESE has been obtained, the
physicist can then apply this information to published
tables which contain relative factors to obtain fetal and/or
organ dose estimates.

At the present time, a device does not exist which
measures ESE directly at the time of the patient x-ray
examination. The objective of the dissertation was to
demonstrate that it is feasible to incorporate a device over
the collimator port so that ESE can be measured for

radiographic and fluoroscopic procedures within an acceptable accuracy. The major emphasis of this research was to design and build the device, and then to study and quantify the factors which affect the calibration of such a device on an overhead radiographic x-ray tube and an undertable fluoroscopic x-ray tube.

The device consists of a parallel-plate transmission ionization chamber, an electrometer, a power supply module and a control unit housing a real-time computational unit for distance corrections, scaling networks and a digital voltage meter. The device was calibrated in units of Roentgen. The device is capable of measuring an exposure range from 1 to 1999 mR and from 1 to 1800 R at a source-to-detector distance of 29.5 cm and a source-to-skin distance of 70.0 cm.

Dosimetry in diagnostic radiology is routinely performed by a medical physicist. In order to obtain the information necessary for an actual dose assessment of a patient, the medical physicist generally requires an assessment of the entrance skin exposure free-in-air (ESE) or some other similar quantity. Exposure is a quantification of the ionization of air. ESE is the measured exposure without backscatter at the entrance plane of the patient's skin (NCRP 1989). Once the measurement of ESE has been obtained, the physicist can then apply this information to published tables which contain relative factors to obtain fetal and/or organ dose estimates (Rosenstein 1976; Rosenstein et al. 1985; Jones and Wall 1985; Rosenstein 1988; Rosenstein et al. 1992; Schultz et al. 1994). Estimates of organs doses can then be used to calculate a patient's effective dose (ICRP 1990; Le Heron 1992; NCRP 1993; Okkalides and Fotakis 1994; Marshall et al. 1994).

The Joint Commission on the Accreditation of Healthcare Organizations (JCAHO) has required that doses from

1

diagnostic radiology procedures be periodically monitored for typical projections in each room and for each x-ray tube (JCAHO 1991). The JCAHO specifically requires for diagnostic procedures, dose be expressed as ESE, except in mammography where ESE is measured and then used to calculate mean glandular dose, and except in computed tomography where computed tomography dose index is required.

The Food and Drug Administration (FDA) issued regulations to implement the Mammography Quality Standards Act of 1992 (MQSA) which required the establishment of a federal certification and inspection program for mammography facilities effective 1994 (Federal Register 1993a). The Senate report on the MQSA states that the standards for accrediting bodies must be no less stringent than those established by the American College of Radiology (ACR). The ACR mammography quality control medical physicist's manual requires measurement of ESE to the breast (ACR 1992). Mean glandular dose is then calculated from the ESE value and relative factors (NCRP 1986).

Federal regulations utilize entrance exposure rates, free-in-air, (EER) to limit the maximum patient exposure rates for fluoroscopic x-ray systems. The regulations state the parameters for measuring compliance of EER limits (Federal Register 1993b). The compliance measurement

positions represent the average adult's skin surface that is nearest to the focus of the x-ray tube.

The FDA issued a public health advisory concerning avoidance of serious x-ray induced skin injuries to patients during fluoroscopically guided procedures (Burlington 1994, FDA 1994). The FDA recommended documentation of radiation dose rates for each fluoroscopic system and for each mode of operation which involved clinically invasive procedures. Measurement of the entrance skin exposure rate, free-in-air, (ESER) was encouraged. EER and ESER are synonymous terms. Estimations of absorbed dose to the skin could then be calculated from the ESER value, the cumulative exposure time and relative factors (Grosswendt 1984).

The Society of Cardiovascular and Interventional Radiology supported the FDA advisory and issued average fluoroscopy times for common fluoroscopically-guided procedures in order to alert physicians to procedures that might require exposure times that would result in skin injury (Pentecost 1994). Wagner et al. (1994) reported on the potential biological effects following high x-ray dose interventional procedures. General principles for minimizing the potential for biological effects were discussed. The authors concluded that ESER is an important parameter in fluoroscopy and that equipment should be tuned to minimize ESER.

ESE measurements are commonly used and reported nationwide as an indicator of the adequacy of a facility's diagnostic procedure. The Nationwide Evaluation of X-ray Trends (NEXT) program, implemented by the Bureau of Radiation Health (BRH), now the Center for Devices and Radiological Health (CDRH) of the Food and Drug Administration (FDA), in collaboration with the state radiation control programs, utilizes the measurement of ESE for selected radiographic procedures and the average ESER for fluoroscopic procedures as indicators of patient exposure (Burkhart et al. 1985; USDHHS 1985; Radiological Health Bulletin 1991). Facilities are encouraged to evaluate their exposure levels for common projections utilized and to compare their exposure levels with the exposure values generally accepted for that projection.

The American Association of Physicists in Medicine (AAPM) described procedures for measuring ESE for common projections and recommended comparing the measured values with national averaged values to indicate if corrective actions were necessary (AAPM 1990). The Conference of Radiation Control Program Directors (CRCPD) urged all state and local radiation control programs to record ESE measurements and to compare them with the values published in its guide so that unnecessary radiation exposure to patients could be reduced (CRCPD 1992).

Currently, several methods are used to estimate ESE in diagnostic radiology and each method has significant drawbacks. A first method to estimate ESE is the documented factor method. This method requires documentation of specific physical, geometric and electronic factors before and after the radiologic procedure. The physical factors include the x-ray equipment utilized for both radiography and fluoroscopy. The geometric factors include the source-to-skin distance (SSD), the source-to-image receptor distance (SID) and the x-ray field size at the SSD or the SID. The electronic factors include the focal spot selection, the image intensifier size selection, the x-ray tube peak potential (kVp), the x-ray tube current (mA), the fluoroscopic cumulative exposure time and the radiographic exposure time or the product of tube current and exposure time (mAs). At some time after the patient irradiation, the medical physicist measures an estimation of the patient's ESE with a dosimeter while recreating the irradiation conditions.

The documented factor method has significant drawbacks when applied to radiography. The radiologic technologist who performs the x-ray examination does not record the physical, geometric and electronic factors of a patient's procedure unless specifically requested to do so. Thus documentation of the factors is seldom done. Errors occur

in estimating and recording the physical, geometric and electronic factors involved in the x-ray examination. Simulation errors occur because of the imprecision of continuously variable generator control parameters and the changes in line voltage compensation which cause variability in the radiation output from the x-ray tube. Thus ESE measurements may not reproduce the actual clinical situation.

Fluoroscopic ESE measurements have several additional drawbacks to the ones listed above for the documented factor method. The x-ray field size, the x-ray tube potential and the x-ray tube current continuously change as the physician chooses different image intensifier sizes and collimation. Due to the changing conditions, only average values of x-ray field size, x-ray tube potential and x-ray tube current can be documented. The documented factor method thus has a significant number of drawbacks for ESE measurements in both radiography and fluoroscopy.

A second method used to estimate ESE involves the use of an exposure-area product meter. Its parallel-plate ionization chamber is mounted to the port of the collimator, and the exposure-area product is measured during the x-ray examination. Several published papers have reviewed the exposure-area product meter and have concluded that a properly calibrated device does an acceptable job of

determining ESE when the dimensions of the x-ray field size are accurately known (Carlsson 1965; Shrimpton and Wall 1982). ESE can be calculated from the exposure-area product measurement by dividing the measurement by the x-ray field area (cm^2) at the patient's surface.

The exposure-area product method has several drawbacks when applied to radiography. An accurate assessment of the x-ray field size at the patient's surface is not routinely documented. If the x-ray field is not collimated so that the entire field impinges on the patient, then both exposure-area product and the calculation of ESE are overestimated. The human body is irregularly shaped and often the rectangularly shaped x-ray field extends beyond the body part of interest. Examples in which the x-ray field typically extends beyond the patient include radiography of the neck, chest and extremities.

The exposure-area product method has limited use in ESE calculations during fluoroscopic examinations. During these examinations, the physician frequently changes the x-ray field size. Thus an average x-ray field size must be assigned which significantly increases the uncertainty of the ESE calculation. Since the exposure-area product method does not measure ESE directly, its use is awkward for the determination of ESE. ESE, EER and ESER are the

measurements required by JCAHO, NEXT, CRCPD and federal and
state regulatory agencies.

A third method used to estimate ESE involves the use of
a device which measures specific geometric and electronic
factors involved in an x-ray examination. Through the use
of a cpmputer program, the above data is applied to
calibration and conversion factors to obtain an estimate of
the ESE. The commercial device is called the PEMNET
(Clinical Microsystems, Inc.; South Arlington, VA).

The PEMNET has several drawbacks. As currently
configured in 1995, the device must be customized in order
to interface with the different equipment designs from the
manufacturers of x-ray equipment. The installation and
calibration of the PENMET is relatively difficult and time
consuming. PENMET recalibration is required when an x-ray
tube is replaced. ESE is not measured but is calculated.
The accuracy of the ESE estimate depends on how close the
calibration factors stored in the computer memory depict the
actual conditions during the irradiation. As the generator
calibration drifts and as the x-ray tube ages, the ESE
estimate may not represent the actual clinical situation.
The system is also relatively expensive. Given the PEMNET
drawbacks, the system would be utilized primarily as a
research tool.

At the present time, a commercial device does not exist which measures ESE directly at the time of the patient x-ray examination. The objective of this study was to demonstrate that it is feasible to incorporate a device over the collimator port so that ESE can be measured for radiographic or fluoroscopic procedures within an acceptable accuracy. The major emphasis of this research was to design and build the device, and then to study and quantify the factors which affect the calibration of such a device on an overhead radiographic x-ray tube and an undertable fluoroscopic x-ray tube.

CHAPTER 2
DOSIMETRY IN DIAGNOSTIC RADIOLOGY

Radiation Quantities

Radiation quantities and their definitions can be confusing especially when the International System of Units (SI) units are mixed with other units of measure. In 1973 and 1974, the International Commission on Radiation Units and Measurements (ICRU) solicited comments from radiation workers concerning the difficulties encountered when shifting to SI units and away from the special units, curie, roentgen and rad. From these comments, it appeared that the majority of workers would find the SI units acceptable if the transition period was sufficiently long (ICRU 1980). The ICRU planned to drop the usage of its special units by 1985. Currently, many Federal and State regulatory agencies in the Unites States along with many equipment manufacturers still use the special units.

Exposure (X) is defined by the ICRU as follows:

$$X = dQ/dm$$

where dQ is the absolute value of the total charge of the ions of one sign produced in air when all the electrons

(electrons and positrons) liberated by photons in air of mass dm are completely stopped in air (ICRU 1980). An alternate definition of exposure (X) is as follows:

$$X = \Psi(\mu_{en}/\rho)(e/W)$$

where Ψ is the energy fluence, μ_{en}/ρ is the mass energy absorption coefficient in air, e is the elementary charge and W is the mean energy expended in air per ion pair formed (ICRU 1980).

The SI unit of exposure is the coulomb per kilogram (C/kg). The special unit of exposure is the roentgen (R) which is defined as follows:

$$1 \text{ R} \equiv 2.58 \times 10^{-4} \text{ C/kg.}$$

Kerma (K) is defined by the ICRU as follows:

$$K = dE_{tr}/dm$$

where dE_{tr} is the sum of the initial kinetic energies of all the charged ionizing particles liberated by uncharged ionizing particles in a material of mass dm (ICRU 1980). Kerma includes energies liberated from bremsstrahlung. An alternate definition of kerma (K) is as follows:

$$K = \Psi(\mu_{tr}/\rho)$$

where Ψ is the energy fluence and μ_{tr}/ρ is the mass energy transfer coefficient (ICRU 1980).

The SI unit of kerma is the joule per kilogram (J/kg). The special name for the unit of kerma is the gray (Gy) which is defined as follows:

$$1 \text{ Gy} = 1 \text{ J/kg.}$$

The special unit of kerma is the rad which is defined as follows:

$$1 \text{ rad} = 10^{-2} \text{ J/kg.}$$

Absorbed dose (D) is defined by ICRU as follows:

$$D = d\epsilon/dm$$

where $d\epsilon$ is the mean energy imparted by ionizing radiation to matter of mass dm (ICRU 1980). An alternate definition of absorbed dose (D) is as follows:

$$D = \Psi(\mu_{en}/\rho)$$

where Ψ is the energy fluence and μ_{en}/ρ is the mass energy absorption coefficient (ICRU 1980). The SI unit of absorbed dose is the J/kg. The special name for the unit of absorbed dose is the gray. The special unit of absorbed dose is the rad.

The mass energy absorption coefficient (μ_{en}/ρ) is related to the mass energy transfer coefficient (μ_{tr}/ρ) as follows:

$$\mu_{en}/\rho = (\mu_{tr}/\rho)(1-g)$$

where g is the fraction of the energy of secondary charged particles that is lost to bremsstrahlung in the material (ICRU 1980). Employing the mass energy transfer coefficient to the definitions of exposure, kerma and absorbed dose, the definitions can be written as follows:

$$X = \Psi(\mu_{tr}/\rho)(1-g)(e/W),$$

$$K = \Psi(\mu_{tr}/\rho) \text{ and}$$
$$D = \Psi(\mu_{tr}/\rho)(1-g).$$

If air is irradiated with photons and if there is no energy liberated by bremsstrahlung during the interactions ($g \to 0$), then exposure can be converted to air kerma. Kerma with no energy liberated by bremsstrahlung is the part of kerma only associated with ionization, and is called collision kerma (Johns and Cunningham 1983). Exposure can always be converted to collision air kerma. Given the above conditions and since the mean value for W_{air}/e was changed from 33.85 J/C (ICRU 1979) to 33.97 J/C (Boutillon and Perroche-Roux 1987; UW-ADCL 1993), then

$$K_{air} \text{ (J/kg)} = X \text{ (R)} \times 0.008764 \text{ [J/(kg R)]},$$
$$K_{air} \text{ (Gy)} = X \text{ (R)} \times 0.008764 \text{ (Gy/R) and}$$
$$K_{air} \text{ (rad)} = X \text{ (R)} \times 0.8764 \text{ (rad/R)}$$

when exposure (X) is measured in roentgen. When exposure (X) is measured in C/kg, then

$$K_{air} \text{ (J/kg)} = X \text{ (C/kg)} \times 33.97 \text{ (J/C)},$$
$$K_{air} \text{ (Gy)} = X \text{ (C/kg)} \times 33.97 \text{ [(kg Gy)/C] and}$$
$$K_{air} \text{ (rad)} = X \text{ (C/kg)} \times 3397 \text{ [(kg rad)/C]}.$$

If no energy is liberated by bremsstrahlung and transient charged-particle equilibrium exists, then air kerma is equivalent to absorbed dose in air and exposure can be converted into either quantity. Charged-particle equilibrium (CPE) exists when the energies, number and

direction of the charged particles are constant throughout
the volume of interest (ICRU 1980). Given the above
conditions and when exposure (X) is measured in roentgen,
then

$$D_{air} \ (J/kg) = X \ (R) \ \times \ 0.008764 \ [J/(kgR)],$$

$$D_{air} \ (Gy) = X \ (R) \ \times \ 0.008764 \ (Gy/R) \ and$$

$$D_{air} \ (rad) = X \ (R) \ \times \ 0.8764 \ (rad/R).$$

When exposure (X) is measured in C/kg, then

$$D_{air} \ (J/kg) = X \ (C/kg) \ \times \ 33.97 \ (J/C),$$

$$D_{air} \ (Gy) = X \ (C/kg) \ \times \ 33.97 \ [(kg \ Gy)/R] \ and$$

$$D_{air} \ (rad) = X \ (C/kg) \ \times \ 3397 \ [(kg \ rad)/C].$$

Exposure can be measured directly. Collision air kerma
can be measured directly. Air kerma can be measured
directly if no energy is liberated by bremsstrahlung. In
order to access how appropriate it is to label a measurement
as air kerma or collision air kerma, one should estimate the
fraction of energy radiated, also known as the
bremsstrahlung yield.

Johns and Cunningham calculated the bremsstrahlung
yield for electrons of different energies interacting in air
(Johns and Cunningham 1983). The equation for the
determination of bremsstrahlung yield (B) is as follows:

$$B = \frac{1}{E_o} \int_0^{E_o} \frac{S_{rad}(E)}{S_{tot}(E)} \ dE$$

where E_o is the initial electron energy, S_{rad} is the energy
loss by bremsstrahlung (radiation stopping power) and S_{tot} is

the total energy loss or total stopping power. The bremsstrahlung yield for the initial electron energies of 20, 40, 60, 80, 100 and 150 keV interacting in air are 0.0001, 0.0003, 0.0004, 0.0005, 0.0007 and 0.0009 respectively. The photon energies generally encountered in diagnostic radiology range from 10 to 120 kev. The maximum electron energy from an interaction with photons in the diagnostic energy range would be 120 kev and the average electron energy would be significantly less. Conservatively stated, the bremsstrahlung yield for the diagnostic energy range is less than 0.0008.

The energy liberated by bremsstrahlung during interactions in air by photons with energies in the diagnostic x-ray energy range is less than 0.08%. The University of Wisconsin Accredited Dosimetry Calibration Laboratory stated that the fraction of energy liberated by bremsstrahlung approaches zero for photons energies below 300 keV (UW-ADCL 1993). A bremsstrahlung yield less than 0.08% is negligible when compared to the $\pm$ 5.0% accuracy of general diagnostic calibration factor. Therefore, direct measurement of air kerma for photon energies in the diagnostic x-ray energy range is appropriate. Currently, Accredited Dosimetry Calibration Laboratories (ADCLs) are reporting calibration factors in both air kerma and exposure (UW-ADCL 1993).

Absorbed dose can be measured directly if the energy liberated by bremsstrahlung is negligible and if charged-particle equilibrium exists. In the discussion above, the energy liberated by bremsstrahlung during interactions of photons in the diagnostic x-ray energy range with air was negligible. Johns and Cunningham (1983) stated that for even approximate charged-particle equilibrium to exist, the percent attenuation of the photons in the range R should be very small.

An approximation of the percent attenuation of photons in the range R was calculated. If the photon energies of interest were 20, 40, 60, 80, 100 and 150 keV, then the corresponding maximum electron energies are 20, 40, 60, 80, 100 and 150 keV respectively. An equation estimating the range (R) of the electron is as follows:

$$R = \int_0^{E_o} \frac{dE}{S_{tot}(E)}$$

where E_o is the initial energy and S_{tot} is the total energy loss or stopping power (Johns and Cunningham 1983). The ranges in air of the electrons listed above are 0.83, 2.7, 5.6, 9.2, 13 and 26 cm respectively. The percent attenuations of photons with energies of 20, 40, 60, 80, 100 and 150 keV in air thicknesses of 0.83, 2.7, 5.6, 9.2, 13 and 26 cm respectively, were calculated to be 0.073, 0.079, 0.13, 0.18, 0.24 and 0.42 respectively.

The percent attenuations of photons in their respective electron ranges were very small. Johns and Cunningham concluded that percent attenuation in the range (R) was very small when the value was less than or equal to 1.2% (Johns and Cunningham 1983). Thus, it is reasonable to state that approximate charged-particle equilibrium exists when photons with energies in the diagnostic x-ray energy range interact in air.

Therefore, it is appropriate to measure directly absorbed dose in air because the energy liberated by bremsstrahlung is negligible and approximate charged-particle equilibrium exists. It is reasonable to conclude, under the conditions of irradiation in air by photons with energies in the diagnostic x-ray energy range, that measurements of collision air kerma, air kerma and absorbed dose in air are equivalent.

Equivalent dose (H_T) is defined by the International Commission on Radiological Protection (ICRP) and the National Council on Radiation Protection and Measurements (NCRP) as follows:

$$H_T = \sum_R (w_R)(D_{T,R})$$

where w_R is the radiation weighting factor and $D_{T,R}$ is the absorbed dose averaged over the tissue or organ (T), due to radiation (R) (ICRP 1991; NCRP 1993). The radiation weighting factor is a dimensionless factor and accounts for

the differences in the relative biological effectiveness
(RBE) of different types of radiation at low doses (ICRP
1991; NCRP 1993). The radiation weighting factor for
photons of all energies is unity (ICRP 1991). The SI unit
for equivalent dose is the J/kg. The special name of
equivalent dose is the Sievert (Sv) which is defined as
follows:

$$1 \text{ Sv} = 1 \text{ J/kg.}$$

Equivalent dose differs conceptually with dose equivalent.
The dose equivalent is based on the absorbed dose at a point
in tissue and weighted by a distribution of quality factors
related to the linear energy transfer of the radiation. The
equivalent dose is based on the average absorbed dose to the
tissue or organ and weighted by a radiation weighting factor
related to the RBE of the radiation.

Effective dose (E) is defined by the ICRP and the NCRP
as follows:

$$E = \sum_{T} (w_T)(H_T)$$

where w_T is the weighting factor for tissue or organ (T) and
H_T is the equivalent dose in tissue or organ (T) (ICRP 1991;
NCRP 1993). The tissue weighting factor is a dimensionless
factor and accounts for the differences in the
radiosensitivity of different tissues and organs. The
effective dose is the sum of the weighted equivalent doses
in all the tissues and organs of the body. The SI unit and

the special name for effective dose are the J/kg and Sievert respectively.

ICRP stated that among the quantities of exposure, kerma, absorbed dose, equivalent dose and effective dose, equivalent dose and effective dose are the quantities intended for use in radiological protection, including the assessment of risks in general (ICRP 1991). ICRP also stated that equivalent dose and effective dose provide a basis for estimating the probability of stochastic effects for absorbed doses well below the thresholds for deterministic effects (ICRP 1991).

Radiation Functions

Radiation functions used in dose calculations include the inverse square law, the percentage depth dose, the tissue-air ratio, the backscatter factor and the ratio of mass energy absorption coefficients. These functions allow a measurement of exposure, collision kerma, kerma or absorbed dose to be shifted to another frame of reference in air, phantom or tissue.

The inverse square law, as related to dosimetry in diagnostic radiology, states that the intensity of photons falling on a flat surface from a point source (focal spot of the x-ray tube) is inversely proportional to the square of

the distance from the point source provided there is no attenuating or scattering material between or near the point source and the flat surface of interest. The inverse square relationship is valid when the dimensions of the radiation source are small compared to the distance between the radiation source and the flat surface of interest.

Nominal focal spot sizes of diagnostic x-ray tubes generally vary in size from 0.1 to 2.0 mm. The distance between the focal spot and the flat surface of interest must be large compared to 0.1 to 2.0 mm in order for the inverse square law to be valid. The inverse square law is commonly utilized in diagnostic radiology for computations in air. Since air interacts with photons, the attenuation and scatter in air should be considered in inverse square law computations where the distances are large and the desired accuracy is high. The percent attenuations of photons with energies of 20, 40, 60, 80, 100 and 150 kev interacting in air with a thickness of 100 cm are 8.46, 2.88, 2.22, 1.98, 1.84 and 1.62 respectively.

The percentage depth dose interrelates doses at points within a phantom. The percentage depth dose depends on the depth in a phantom, the area of the photon field, the distance from the source of the radiation to the surface of the phantom, and on the quality of the radiation. The equation for the percentage depth dose (P) is as follows:

$$P = 100 \times (D_x/D_y)$$

where D_x is the dose at the point of interest and D_y is the
dose at the reference point (Johns and Cunningham 1983).
The reference point in a phantom is often the depth of
maximum dose.

Harrison (1981) published tables of percentage depth
doses in water measured for a range of x-ray field sizes and
beam qualities corresponding to irradiation conditions
encountered in diagnostic radiology where x-ray tubes with
tungsten anodes were utilized. The author showed the that
characterization of radiation quality by only the first
half-value thickness (HVT) was inadequate and would lead to
increased uncertainties especially at depths greater than 10
cm. Harrison recommended and Carlsson and Carlsson (1984)
concluded that the quality of radiation be specified in
terms of both the x-ray tube peak kilovoltage potential
(kVp) and the first HVT in order to better characterize, in
a practical manner, the x-ray spectrum encountered.

The tissue-air ratio is the ratio of the dose on the
central ray of the primary beam and at a point of interest
in a phantom to the exposure or dose at the same point of
interest in air. The tissue-air ratio depends on the depth
below the surface of the phantom, the area of the photon
field at that phantom depth, and on the quality of the

radiation. The equation for the tissue-air ratio (T_a) is as follows:

$$T_a = D_x/D_{x'}$$

where D_x is the phantom dose at a point of interest and $D_{x'}$ is the dose to air at the same point of interest (Johns and Cunningham 1983). Unlike the percentage depth dose, the tissue-air ratio is independent of the source-to-surface distance.

Schulz and Gignac (1976) measured tissue-air ratios for 70 to 120 kVp x rays filtered by a total of 2.5 and 3.5 mm aluminum under conditions that simulated those in diagnostic radiology. The tissue-air ratios were expressed in terms of rads-to-water per roentgen. The authors also outlined a method to estimate the fetal dose using tissue-air ratios.

Harrison (1983) calculated tissue-air ratios from measurements of percentage depth doses and backscatter factors in water for a range of x-ray field sizes and beam qualities corresponding to irradiation conditions encountered in diagnostic radiology where x-ray tubes with tungsten anodes were utilized. The tissue-air ratios were expressed in terms of rads per roentgen. The author emphasized the need to specify radiation quality in terms of both kVp and the first HVL.

The backscatter factor is a special case of the tissue-air ratio. When the dose at the point interest in the

phantom is equal to the maximum dose in the phantom, the
tissue-air ratio reduces to the backscatter factor. Thus
the backscatter factor is the value by which the dose in air
is increased by the radiation scattered back from the
phantom (Johns and Cunningham 1983). For photons in the
diagnostic x-ray energy range, the depth of the maximum dose
in the phantom approaches zero, so that the maximum dose is
on the surface of the phantom.

Harrison (1982) measured backscatter factors for water
for a range of x-ray field sizes and beam qualities
corresponding to irradiation conditions encountered in
diagnostic radiology where x-ray tubes with tungsten anodes
were utilized. The author utilized a cylindrical ionization
chamber and thermoluminescent dosimetery for the
measurements. The author concluded that the experimental
results were within ±3% of the reported values found in the
British Journal of Radiology Supplement 17.

Grosswendt (1984) calculated backscatter factors for
cylindrical phantoms of various compositions including
water, graphite and acrylic glass using Monte Carlo
methodology. Attempts were made to simulate radiation
qualities encountered in diagnostic radiology. The
backscatter factors were expressed in terms of a ratio of
the kerma rate to water at the surface of a water phantom to
the kerma rate to water at the same point in space in the

absence of a phantom. The author concluded that the experimental results from Harrison (1982) were somewhat higher than the theoretical values presented. Grosswendt (1990) applied the same techniques to extend the calculations to higher radiation qualities and different irradiation geometries.

Klevenhagen (1989) measured backscatter factors with a thin parallel-plate ionization chamber using water as the scattering medium. A range of radiation qualities and x-ray field sizes were utilized to simulate conditions encountered in diagnostic radiology. The backscatter factor was expressed in terms of the ratio of the exposure at the surface of the phantom to the exposure at the same point in space in the absence of the phantom multiplied by the ratio of the mass energy transfer coefficients for water and for air in the presence of scattering medium and in free space. The author concluded that the measurement results confirm the theoretical calculations of Grosswendt.

The Institute of Physical Sciences in Medicine (IPSM) working party acknowledged that values of backscatter factors for x-ray energies below 140 kVp reported in the British Journal of Radiology Supplement 17 appeared to be inaccurate (IPSM 1991). The IPSM working party recommended that new values based on the Monte Carlo calculations from

Grosswendt be used for radiation qualities up to 8 mm aluminum HVL in radiation therapy.

Schultz et al. (1994) calculated backscatter factors utilizing the ADAM and EVA mathematical models developed by Kramer et al. (1982), for three different x-ray energy spectra. The projection utilized was for the posterior-anterior chest radiograph. The backscatter factors were expressed in terms of the ratio of absorbed dose at the phantom surface to air kerma. The authors concluded that the backscatter factor increases with increasing x-ray energy.

The ratio of averaged mass energy absorption coefficients can be used to relate absorbed dose in a medium to another medium under conditions of charged particle equilibrium and irradiation with the same photon energy spectrum. An equation relating the absorbed dose in a medium (D_{medium}) to that in air (D_{air}) is as follows:

$$D_{medium} = D_{air} \frac{(\mu_{en}/\rho)_{medium}}{(\mu_{en}/\rho)_{air}}$$

where μ_{en}/ρ is the mass energy absorption coefficient for that particular material (Wall et al. 1988). While mass energy absorption coefficients depend on photon energy, averaged mass energy absorption coefficients in muscle weighted for typical x-ray energy spectra are very similar. Wall et al. (1988) concluded that the ratio of the averaged

mass energy absorption coefficients of muscle to air was 1.06 ± 1% for all typical diagnostic x-ray qualities.

Monte Carlo Derived Conversion Coefficients

Monte Carlo methodology as applied to diagnostic radiology is based upon the simulation of the transport of photons, having an energy spectrum similar to an x-ray energy spectrum from an diagnostic x-ray tube and a field size corresponding to those utilized in diagnostic radiology, through a anthropomorphic mathematical model. The mathematical models utilized are designed to have similar characteristics to that of average humans. The deposition of energy and the location are recorded from the photon interactions in the phantom. The histories of the energy deposition from many photons are summed for the different locations that define the tissues or organs of interest. Conversion factors or coefficients which relate the tissue or organ dose of interest to the entrance skin exposure (free-in-air) or surface dose to the phantom are then calculated.

There are several sources for error in the Monte Carlo calculations as they are applied to patient dosimetry in diagnostic radiology. The mathematical models utilized must precisely define, in three dimensions, the tissue and organ

boundaries of interest. The unique anatomy of a patient may not conform to that of the model. Mathematical models are generally composed of only three tissue types consisting of soft tissue, lung and skeleton. Thus the composition and density of patient tissues and organs may not be adequately simulated by the interaction coefficients assigned to them. The photon interaction coefficients have uncertainties associated with their known values. The number of photon histories computed must be finite which produces statistical uncertainties. Lastly, the x-ray energy spectrum, the x-ray field size and the x-ray field location on the model utilized in the Monte Carlo calculations may not be similar to the patient irradiation conditions.

Rosenstein (1976) published Monte Carlo calculations of organ doses in diagnostic radiology. The author employed the use of the Medical Internal Radiation Dose Committee MIRD-5 adult mathematical model. The MIRD-5 model represented a hermaphrodite adult. The height and mass of the whole body, as well as the masses of the internal organs were based on the ICRP Reference Man data (ICRP 1975). The body tissues were composed of soft tissue, lung and skeleton (ICRU 1992).

Rosenstein et al. (1985) published Monte Carlo calculations of glandular tissue doses in mammography. The authors modeled different breast compositions, thicknesses

and compressions. The units employed for the conversion coefficients were glandular tissue absorbed dose in millirad per unit ESE in roentgen. Irradiation conditions were characterized by descriptions of breast composition, degree of breast compression, compressed breast thickness, projection, SID, HVL, x-ray tube anode composition and filtration. The NCRP stated that when allowances are made for methodological differences, the calculated values are in good agreement with those obtained from physical phantom measurements (NCRP 1986).

Jones and Wall (1985) published Monte Carlo calculations of organ doses from medical x-ray examinations. The authors utilized the ADAM and EVA mathematical models developed by Kramer et al. (1982). The ADAM model added testes to the MIRD-5 model and modified the neck region to improve estimates of thyroid doses. The EVA model was proportionally 0.83 times smaller than the ADAM model, with testes excluded and with ovaries, uterus and female breasts included. The body tissues were composed of soft tissue, lung, skeleton and skin (ICRU 1992). The conversion coefficients were defined as the mean organ absorbed dose per unit entrance surface dose with backscatter. Irradiation conditions were described by patient position and projection, x-ray field size at midplane, SSD, percentage of primary beam striking the model, HVL and kVp.

Rosenstein (1988) published Monte Carlo calculations of selected tissue doses for projections common in diagnostic radiology which superseded Rosenstein (1976). The author employed the use of an updated MIRD-5 adult male and female mathematical model. The units used for the conversion coefficients were tissue absorbed doses in millirad per unit ESE in roentgen. The calculated tissue dose values were the average absorbed dose in tissue that was weighted over its entire mass. Irradiation conditions were characterized by descriptions of patient position and projection, x-ray field size at the film, SID and HVL. The authors stated that the average absorbed dose in the uterus could be used to approximate the absorbed dose in the embryo during the first two months of pregnancy.

Rosenstein et al. (1992) published Monte Carlo calculations of selected tissue doses for the upper gastrointestinal fluoroscopic examination. The authors utilized the ADAM and EVA mathematical models developed by Kramer et al. (1982). The units used for the conversion coefficients were tissue absorbed doses in millirad per unit ESE in roentgen. The calculated tissue dose values were the average absorbed dose in tissue that was weighted over its entire mass. Irradiation conditions were characterized by descriptions of patient position and projection, x-ray field size at the image receptor, SID, SSD and HVL. The authors

stated that the average absorbed dose in the uterus could be used to approximate the absorbed dose in the embryo during the first two months of pregnancy.

Schultz et al. (1994) published Monte Carlo calculations of dose conversion factors for chest radiography of adults with a relatively high energy x-ray spectrum. The authors utilized the ADAM and EVA mathematical models developed by Kramer et al. (1982). The units used for the conversion coefficients were organ absorbed dose in gray per unit air kerma, free-in-air in gray. Irradiation conditions were characterized by descriptions of patient position and projection, SID, SSD, HVL or filtration and kVp. Effective dose and effective dose equivalent per unit air kerma, free-in-air were also calculated. The effective dose was 60 to 70% of the effective dose equivalent for the same irradiation conditions. The authors concluded that when dose conversion factors are reported, the configuration and exposure conditions for which they are valid should be well described.

Seuntjens et al. (1987) showed the necessity of beam specification by two parameters, HVL and kVp, for accurate determination of the exposure-to-dose conversion factor especially in the diagnostic quality range. In addition, Harrison (1981) recommended and Carlsson and Carlsson (1984)

concluded that the quality of radiation be specified in terms of both the kVp and the first HVT in order to better characterize, in a practical manner, the x-ray spectrum encountered.

RANDO Phantom Derived Conversion Coefficients

Anthropomorphic phantom methodology as applied to diagnostic radiology is based upon dosimetric measurement in a physical phantom after irradiation from x rays generated by diagnostic radiology equipment. The RANDO phantom (Alderson Research Laboratories, INC.; Stamford, CT) is one of the most commonly used physical phantoms. The RANDO phantom is a solid, anthropomorphic phantom representing the head, thorax and pelvic portions of either an adult male or female. The phantom has soft tissues made with isocyanate rubber-based muscle substitute, lungs made with solid RANDO lung substitute and a human skeleton (ICRP 1992). The entire phantom is cut into thin transverse sections. The sections contain a matrix of holes for placement of dosimeters. Thermoluminescent dosimeters (TLDs) are well-suited for this purpose. Conversion coefficients are then calculated which relate organ or tissue dose of interest to ESE or surface dose to the phantom.

There are several sources of error in the physical phantom derived conversion coefficients as they are applied to patient dosimetry in diagnostic radiology. The physical phantom utilized must precisely define, in three dimensions, the tissue and organ boundaries of interest. The unique anatomy of a patient may not conform to that of the phantom. Physical phantoms are generally composed of only one to four tissue types. Thus the composition and density of patient tissues and organs may not be adequately simulated. Uncertainties in the measurements associated with thermoluminescent dosimetry are due to phosphor differences in sensitivity to irradiation, differences in mass energy absorption coefficients in relation to tissue, fading of the latent signal with time, fluctuations in the reader performance and calibration errors. Lastly, the x-ray energy spectrum, the x-ray field size and the x-ray field location on the physical phantom may not be similar to the patient irradiation conditions.

Gray et al. (1981) measured normalized organ doses for 24 diagnostic examination projections. The organs of interest were the uterus, ovaries, testes, eyes, thyroid and active bone marrow. The authors utilized an Alderson RANDO phantom and lithium fluoride and calcium fluoride TLDs. The units used for the conversion coefficients were organ absorbed dose in millirad per unit ESE in roentgen.

Irradiation conditions were characterized by descriptions of phantom position and projection, x-ray field size at the image receptor, SID, HVL and kVp. The authors concluded that significant reduction in dose to specific organs is possible by properly choosing the projections (anterior-posterior or posterior-anterior).

Marshall and Faulkner (1993) measured normalized organ dose as a function of field size for abdominal examinations. The organs of interest were those that were specified with tissue weighting factors by the ICRP (1991). The method used lithium fluoride TLDs and an Alderson RANDO phantom. The units for the conversion coefficients were water absorbed dose in gray per unit water entrance surface absorbed dose with backscatter in gray. Irradiation conditions were characterized by descriptions of projection, x-ray field size, SSD, SID, kVp and HVL. The authors concluded that the conversion coefficients were strongly dependent on whether organs were directly in the primary x-ray beam which in turn was dependent on the field size and projection direction.

Embryo and Fetal Dosimetry

NCRP stated that it was the responsibility of the prescribing physician to explain all treatment procedures to

the patient, especially any procedure that may present a significant risk (NCRP 1994). Before a procedure is begun, knowledge of pregnancy or possible pregnancy should be obtained and then considered in the risk-to-benefit analysis of the procedure. The risk-to-benefit analysis of a radiologic procedure should include consideration of deterministic and stochastic effects.

Radiation induced deterministic effects, formerly called nonstochastic effects, are defined as somatic effects which increase in severity with increasing radiation dose above a threshold dose (NCRP 1993). Radiation induced deterministic effects on the mammalian embryo and fetus include lethality, gross malformation, growth retardation, sterility, cataracts, neuropathology, mental retardation, mental impairment and small head size (NCRP 1994). Radiation induced stochastic effects are defined as one in which the probability of the effect occurring increases continuously with increasing absorbed dose while the severity of the effect, in affected individuals, is independent of the magnitude of the absorbed dose (NCRP 1993). Stochastic effects are an all-or-none response. Radiation induced stochastic effects on the mammalian embryo and fetus include cancer and hereditary disorders (ICRP 1991).

Embryo and fetal risks associated with irradiation from diagnostic radiology procedures depends on the conception age and the amount of radiation absorbed. NCRP (1994) summarized the temporal relationship of possible effects of radiation during pregnancy in the following manner. In the first 9 days after conception, the effect was resorption of the embryo or lethality. During days 9 to 14 postconception, the demonstrated effects included lethality and growth retardation. During days 15 to 50 postconception, the effects of highest incidence included gross malformations, growth retardation and neuropathology. In the days 55 to 105 postconception, the effects of highest incidence included growth retardation, sterility, mental retardation, mental impairment and small head size. During the days 105 to 175 postconception, the effects of highest incidence included growth retardation, sterility and mental retardation. In the days 175 to 280 postconception, the readily apparent effects included growth retardation and sterility. Subsequent cancer development was a demonstrated effect in days 15 to 280 postconception.

Stovall et al. (1995) summarized the radiation induced risk to the embryo or fetus as a function of dose in the following manner. If the absorbed dose was less than 0.05 Gy, then there was little risk of damage. If the absorbed dose was 0.05 to 0.10 Gy, then the risk was uncertain. If

the absorbed dose was 0.10 to 0.50 Gy, then there was significant risk of damage during the first trimester. If the absorbed dose was greater than 0.50 Gy, then there was high risk of damage during all trimesters.

NCRP (1994) concluded that exposures resulting in 100 mSv or less would not cause detectable deterministic effects in the embryo or fetus, with the possible exception of the induction of small head size with a threshold of perhaps as low as 50 mSv. The NCRP also concluded that the stochastic effects should not exceed 1% for an acute exposure resulting in 100 mSv to the embryo or fetus.

Wagner et al. (1985) recommended the following guidelines for pregnancy termination associated with embryo or fetal exposure to diagnostic radiology procedures. If received during the first two weeks after conception, exposure to diagnostic radiation was not an indication for therapeutic abortion. If received after the second week and through the seventh week postconception, therapeutic abortion based solely on radiation exposure was not advised for doses less than 15 rads, unless there were other compromising factors severely threatening either the mother or conceptus. For conceptus exposure during the eighth week through the fifteenth week, and at doses above 15 rad, therapeutic abortion could be advised but not necessarily recommended based solely upon radiation exposure. For fetal

exposure after the fifteenth week postconception, the pregnancy should be carried to term.

Brent (1983) stated that the risks from an acute exposure resulting in 1 to 5 rad to the embryo were far below the natural spontaneous risks of the developing embryo. The cited spontaneous risks of a developing embryo were a spontaneous abortion rate of 25 to 50%, a major malfunction rate of 2.7 to 3.0%, a intrauterine growth retardation rate of 4% and a genetic disease rate of 8 to 10%. A maximum risk of approximately 0.1% was attributed from an acute exposure which resulted in 1 rad to the embryo. The author concluded that there was no justification for terminating a wanted pregnancy because of a radiation hazard, when the embryo absorbed dose was 5 rad or less. Brent also concluded that superficial evaluations of radiation exposures were a disservice to the patient and an example of poor medical care.

Wagner et al. (1985) concluded that if pregnancy was not suspected during the radiological procedure, then the patient should be advised of the actual dose received by the conceptus and of the radiation risks involved. NCRP (1994) indicated that if an unintended exposure of the embryo or fetus occurs, then the magnitude of the exposure to the embryo or fetus should be determined promptly and recorded. NCRP recommends that actions be instituted to assure that

the conceptus dose estimation is accurate and that expert medical evaluation, advise and follow-up be utilized on a case-by-case basis.

Several authors have developed different techniques to estimate fetal dose from exposure to diagnostic radiology procedures for the case when the fetus was in the field-of-view or primary x-ray beam. Each technique required that certain data be documented before and after the diagnostic procedure. The dose to the fetus was assumed to be the same as the dose to the uterus (ICRP 1991; NCRP 1994).

Ragozzino et al. (1981) estimated fetal absorbed dose from common abdominal and pelvic radiographic examinations. The method used localization of the fetus with ultrasound, knowledge of the patient's irradiation parameters and application of the normalized depth dose to estimate the absorbed dose to the fetus. Uterine depth dose was experimentally determined for different x-ray tube potentials in an Alderson RANDO phantom. The units for the normalized depth dose were uterine absorbed dose in rad per unit ESE in roentgen. ESE of the patient was measured by reproducing the conditions of the patient exposure. The authors concluded that selection of projection (posterior-anterior) and adjustment of bladder volume could result in significant fetal dose reduction, particularly in the first trimester.

Wagner et al. (1985) described a method to estimate fetal absorbed dose. The method used percent depth dose tables from Harrison (1981), depth of the conceptus and knowledge of irradiation parameters including kVp, HVL, field size and entrance absorbed dose at the skin surface over the conceptus. If ESE was measured, then a backscatter factor as found in tables similar to Harrison (1982) was employed. The author concluded that this method to calculate fetal absorbed dose allowed for simple interpolation of numerous HVLs and kVps. Another method was also described by the author which employed the use of tissue-to-air ratio tables from Schulz and Gignac (1976).

Clarkson et al. (1987) described a method utilizing a computer program to estimate fetal absorbed dose. The method used values of conversion coefficients from the Monte Carlo calculations of Rosenstein (1976), knowledge of irradiation conditions including kVp, HVL, projection, field size and ESE over the conceptus. Sources of inaccuracies of the absorbed dose estimation were discussed and included anatomical differences between the patient and the phantom, and the variations in the size, shape and position of the uterus as pregnancy progresses. The author concluded that when circumstances require that an estimate of fetal absorbed dose be determined, the result was usually needed

with some clinical urgency. The use of the computer program allowed for rapid calculation of fetal absorbed dose.

Wagner et al. (1985) described a method to estimate fetal absorbed dose from exposure to diagnostic radiology procedures for the case when the fetus was out of the field-of-view or primary x-ray beam. The method used values of the out-of-field percent depth dose, values of the backscatter factor, depth of conceptus, distance from conceptus to the edge of the x-ray field and knowledge of irradiation conditions including kVp, HVL and ESE. The author concluded that if the position of the conceptus was more than 10 cm from the edge of the x-ray field, then a rule of thumb was that the conceptus dose was less than 2% of the entrance absorbed dose.

Adult Dosimetry

NCRP stated that it is the responsibility of the prescribing physician to explain all treatment procedures to the patient, especially any procedure that may present a significant risk (NCRP 1994). The risk-to-benefit analysis of a radiologic procedure should include consideration of deterministic and stochastic effects. Radiation induced deterministic effects relevant to an adult patient undergoing a diagnostic radiology procedure include opacity

of the lens of the eye, temporary sterility, depression of hematopoiesis, skin erythema and epilation. The threshold dose equivalents for opacity of the lens of the eye, temporary sterility, depression of hematopoiesis, skin erythema and epilation from an acute exposure are 0.5 to 2.0, 0.15, 0.5, 3 to 5, and 3 to 5 Sv respectively (ICRP 1991). Radiation induced stochastic effects are considered to be the principle effect that may occur to an adult following exposure to low doses of ionizing radiation (NCRP 1993).

Wagner et al. (1994) measured skin absorbed doses for several interventional radiology procedures. Absorbed dose was estimated by using either TLD or measuring ESE and applying backscatter factors. A documented neurologic embolization procedure resulted in a skin absorbed dose of 18 Gy. The authors concluded that proper management of patients requires efforts to minimize radiation exposure and that high-dose procedures should be documented.

Fife et al. (1994) estimated ovarian absorbed dose for a hysterosalpingographic procedure. The method used TLD to determine entrance dose, measurements of ESE, values of backscatter factors from Wall et al. (1988), Monte Carlo derived conversion coefficients from Rosenstein and knowledge of irradiation conditions including HVL and x-ray field size.

Le Heron (1992) estimated effective dose resulting from 22 different x-ray examinations. The method used measurements of dose-area product, Monte Carlo derived conversion coefficients from Jones and Wall (1985) and knowledge of irradiation conditions including kVp, HVL and field size. The mean remainder dose was an mass-weighted mean of ten organs listed in ICRP (1990). The author stated that calculations of effective dose equivalent depended strongly on the method used to determine the remainder dose and hence there was little purpose in presenting such data.

Okkalides and Fotakis (1994) estimated effective dose resulting from 40 different types of radiographic procedures. The method used measurements of ESE, Monte Carlo derived conversion coefficients from Wall et al. (1988) and knowledge of irradiation conditions including kVp, HVL and x-ray field size. Effective dose was calculated with the assumption that the remainder dose was negligible.

Marshall et al. (1994) conducted a comparison of radiation dose in examination of the abdomen using different radiological imaging techniques. The method used TLD to determine entrance dose, RANDO phantom conversion coefficients from Marshall and Faulkner (1993) and knowledge of irradiation conditions including kVp, HVL and x-ray field size. Effective dose and effective dose equivalent were

calculated. The authors showed that the calculation of effective dose equivalent was critically dependent on how the remainder dose was specified. The organs consisting of the stomach, liver and colon received the highest dose but had to be included in the remainder dose because those organs were not designated with separate weighting factors. The remainder dose specification problem was greatly reduced in the calculation of effective dose since the stomach, liver and colon had specified tissue weighting factors. The authors concluded that anterior-posterior (AP) projections resulted in higher effective doses than did posterior-anterior (PA) projections and this was due to the majority of the radiosensitive organs in the abdomen, such as the stomach, colon and liver, being closer to the entrance surface for AP projections compared with PA projections.

CHAPTER 3
INSTRUMENTATION FOR MEASUREMENT OF RADIATION

Instrumentation for measurement of radiation in the diagnostic radiology energy range commonly involves the use of devices which collect the charges produced by ionization. The device's signals produced upon irradiation are proportional to the charges collected. Once the devices are properly designed and calibrated, measurements of exposure, collision air kerma, air kerma, absorbed dose in air or absorbed dose in tissue can be determined and then applied to patient dosimetry and quality control techniques.

Standard Free-Air Ionization Chambers

The standard free-air ionization chamber is used as a standard in calibration laboratories (Hendee 1984; Sprawls 1987). The standard free-air ionization chamber is a primary standard that was designed to measure radiation exposure expressed in Roentgen (Ter-Pogossian 1967). Consequently, the device must precisely define a mass of air and collect and measure all the charges produced from

ionization in that mass of air upon irradiation with photons.

The standard free-air ionization chamber is a parallel plate design. The design utilizes a guard ring around the collection electrode plate to establish a uniform electric field throughout the sensitive volume of air and to precisely define the boundaries of the sensitive volume of air (Meredith and Massey 1977). The guard ring consists of an air gap and a grounded electrode plate which surrounds the collection electrode plate.

The free-air ionization chamber is also designed so that its electrode plates are not in physical contact with the sensitive volume of air. An air buffer region extends beyond the sensitive volume and surrounds the device's electrodes which prevents any x-ray interactions with the electrodes from influencing the quantity of ionization in the sensitive volume region. A potential difference is applied between the electrode plates to achieve saturation and the charges produced from ionization upon photon irradiation are collected. Saturation is achieved when all the charges produced from ionization are collected and none recombine. The ionization current is measured by an electrometer.

The distance between each electrode plate and the sensitive volume of air must be larger than the maximum

range of the electrons liberated by the photon interactions in air to ensure that the electrons expend all their energy before collection (Meredith and Massey 1977; Hendee 1984) and to ensure charged particle equilibrium (Ter-Pogossian 1967). Several consequences occur as the photon energy is increased. The consequences include an increase in the range of the electrons in air which necessitates an increase in the electrode plate separation distance which in turn increases in the thickness of air, the photon attenuation and the photon attenuation correction factor. For these reasons, the standard free-air ionization chamber should not be used for photon energies greater than 3 MeV (Johns and Cunningham 1983; Hende 1984).

The main advantage of the standard free-air ionization chamber is that it is used as a primary standard for measuring exposure. The disadvantages of the standard free-air ionization chamber include the lack of mobility resulting from its relatively large size and weight; the difficulties associated with its set-up and usage; and the potential for electrical hazard to personnel.

Thermoluminescent Dosimeters

Thermoluminescence is the emission of light by the application of heat. Thermoluminescent dosimeters (TLDs)

are based on the principle that, when certain crystalline inorganic materials are heated, light is emitted which is proportional to the amount of radiation energy previously absorbed by the materials.

The thermoluminescence mechanism was discussed by Knoll (1979). The crystalline structure of thermoluminescent material has imperfections in the lattice that act as trapping centers for electrons and holes. When the material is irradiated, energy is absorbed which raises some electron energies from the valence energy band to the conduction energy band were some electrons are captured by trapping centers. Holes are trapped by an analogous process. Trapping centers for electrons and holes reside in the forbidden energy gap between the valence energy band and the conduction energy band.

If the energy difference between the conduction band and the trapping center is sufficiently large, then there is only a small probability per unit time at ordinary room temperatures that the electrons will escape the trap by being thermally exited (Knoll 1979). Upon heating of the material, the trapped electrons gain enough thermal energy so that they are re-excited back to the conduction energy band from which the electrons can return to the valence energy band and recombine with holes resulting in the emission of light. The amount of light emitted is

proportional to the number of electrons and holes trapped which in turn is proportional to the amount of energy absorbed from the irradiation (Johns and Cunningham 1983).

The TLD reader is a device that heats the TLD and detects the subsequent emission of light through the use of a photomultiplier tube. The light yield is recorded as a function of temperature in a glow curve. The area under the glow curve is proportional to the total number of photons emitted by the TLD. The different peaks in a glow curve correspond to the different energy levels of the trapping centers. If the TLD is raised to a relatively high temperature in a process called annealing, all the trapping centers are depleted, the exposure record is erased and the TLD is ready to be reused (Knoll 1979).

TLD phosphors differ according to their trap depths. Sensitivity of a TLD phosphor is a function of the number of trapped electrons and holes per unit absorbed dose. If the traps are shallow, indicating that the energy differences between the trapping centers for electrons and the conduction band are small, the number of electrons and holes trapped per unit absorbed dose can be relatively large. Shallow traps are more susceptible to fading than deep traps. Fading is the loss of trapped electrons and holes due thermal excitation at ordinary room temperatures. Johns and Cunningham (1983) stated that lithium fluoride may be

used to measure absorbed dose over a wide range (10^{-5} to 10^{3} Gy) and that lithium fluoride was relatively dose-rate independent.

TLD phosphors also differ according to their mass energy absorption coefficients. Ideally for diagnostic radiology dosimetry, the TLD phosphor should have an identical photon energy response as that of soft tissue over the range of photon energies encountered in diagnostic radiology. Wall et al. (1988) discussed the tissue equivalence of TLD phosphors and demonstrated that none of the commercially available phosphors fulfilled this ideal. The author stated that lithium borate was the most tissue-equivalent phosphor commercially available.

The precision of a TLD measurement depends on the random uncertainties including the variations in the thermoluminescent mechanism, the variations in the phosphor material, the variations in the reader mechanism and the variations in the calibration procedures. Johns and Cunningham (1983) stated that with great care, a precision of approximately 2% was possible. The accuracy of a TLD measurement depends on the systematic uncertainties including fading, non-linear dose-response relationships and differences in the relative photon energy responses.

The advantages of thermoluminescent dosimetry include the availability of many different sizes and shapes of

phosphors allowing for placement in small spaces; the ability to measure absorbed dose directly; and the ability to measure absorbed dose over a wide range.

The disadvantages of thermoluminescent dosimetry include the delay between the irradiation and the absorbed dose determination; the difficulties associated with calibration against reference ionization chambers; the difficulties associated with annealing, fading and handling of the TLDs; the differences in the phosphor's mass energy absorption coefficients relative to soft tissue producing a different photon energy response; and the possibility of casting a shadow-artifact on a radiograph during clinical procedures. TLDs measure absorbed dose with backscatter directly, not exposure or ESE.

Practical Ionization Chambers

Practical ionization chambers were developed for routine use to measure exposure. The practical ionization chamber is based on the fact that ions produced by the irradiation of a known mass of air can be collected in an efficient manner so that the charge collected per unit air mass yields an exposure measurement. The practical ionization chamber utilizes an air-equivalent wall. By proper choice of the wall material and thickness, it is

possible to produce a practical ionization chamber which has an energy response similar to that of air.

Ideally, an air-equivalent wall is composed of materials that have mass energy absorption coefficients identical to those of air. Since it is not possible to construct the ideal air-equivalent wall, nearly air-equivalent walls over a broad energy range have been constructed (Ter-Pogossian 1967). Two approaches to evaluate if compounds or mixtures have similar photon absorptions they are the interaction data method (White 1977b and 1978) and the effective atomic number method (Spiers 1946; Weber and van den Berge 1969; White 1977a, 1977b; 1978; Hende 1984; Waggener et al. 1985; Johns and Cunningham 1983).

The interaction data method employs the use of photon interaction coefficients to summarize a compound or mixture characteristics upon photon irradiation. The interaction data method evaluates the important photon interaction processes at the energy range of interest. The important photon interaction processes in the diagnostic energy range includes the photoelectric effect, incoherent (Compton) scattering and coherent (Rayleigh) scattering. The photon interaction processes of interest in the application of depositing energy in a ionization chamber over the

diagnostic energy range are the photoelectric effect and incoherent scattering.

The interaction data method uses the addition rule in which a compound or mixture photon interaction mass attenuation coefficient for a particular interaction process is equivalent to a sum of its elemental interaction coefficients weighted according to the elemental proportion by weight. The interaction data method is used as the gold standard for the simulation of tissue substitutes (White 1978).

The concept of effective atomic number is useful when the photoelectric process is dominate over the Compton process, which occurs at the photon energies encountered in diagnostic radiology (Johns and Cunningham 1983). In the photon energy range where the Compton process is dominate, photon absorption is relatively independent of atomic number and dependent on the number of electrons per gram in the mixture (Johns and Cunningham 1983). The electron density of the mixture is another important factor to consider in selecting the components in a mixture for an air-equivalent wall.

The effective atomic number of a mixture is a single number which attempts to characterize the magnitude of the photoelectric interaction process. The ratio of the components in a mixture is selected so that the mixture's

effective atomic number is identical or nearly identical to
that of air. Johns and Cunningham (1983) calculated the
effective atomic number of air to be 7.78. If the effective
atomic number of a practical ionization chamber's wall is
less than that of air, the relative response from the
practical ionization chamber upon irradiation with photons
in the diagnostic energy range should be less than that of
the standard free-air ionization chamber. Conversely, if
the effective atomic number is greater than that of air, the
relative response from the practical ionization chamber upon
irradiation with photons in the diagnostic energy range
should be greater than that of the standard free-air
ionization chamber.

The practical ionization chamber, in an analogous
manner, replaces the relatively large thickness of air used
in the standard free-air ionization chamber with an air-
equivalent wall. The thickness of the air-equivalent wall
should be larger than the maximum range of the electrons
liberated by the photon interactions to ensure charged
particle equilibrium. Johns and Cunningham (1983) discussed
the relative response from a practical ionization chamber
upon photon irradiation as the chamber wall thickness was
varied. The authors observed that as the wall thickness was
increased, the relative response rose to a maximum when the
equilibrium wall thickness was attained, and then fell

slowly. The reduction in the relative response for a wall
thickness beyond the equilibrium wall thickness was due
photon attenuation in the wall.

The practical ionization chamber must be calibrated
against a standard free-air ionization chamber to determine
its energy dependent response (Hendee 1984). Typically, the
response of the practical ionization chamber is compared at
several photon energies to the response of the reference
ionization chamber to determine the calibration factors.

The practical ionization chamber collects the charges
in the sensitive volume by the application of a potential
difference between the electrodes. The magnitude of the
potential difference that is necessary to achieve saturation
is a function of the distance between the electrodes, the
exposure rate and the geometric shape of the sensitive
volume. Waggener et al. (1985) stated that the general
recombination of ions within a practical ionization chamber
should be kept to a practical minimum and that under
ordinary conditions the recombination should not exceed 1%.

An electrometer is a device that measures the small
currents (10^{-12} to 10^{-9} ampere) produced in a practical
ionization chamber. Since charge is not measured directly,
the electrometer measures the voltage developed on a known
capacitor, which serves as a current integrator. An
electrometer and a practical ionization chamber can be

calibrated so that the output is in units of exposure, collision air kerma, air kerma or absorbed dose in air.

The advantages of the practical ionization chamber include the relative ease of mobility resulting from its small size and weight; the relative ease associated with its set-up and usage; the durability of its construction; and the precision and accuracy of its measurement. The disadvantages of the practical ionization chamber include the necessary calibration on a yearly basis to access its energy dependent response; the loss of current due to insulator leakage; and the offsets associated with electrometer measurements.

CHAPTER 4
DESIGN OF THE PROTOTYPE DEVICE

The design of the prototype device is based on a
practical ionization chamber. Figure 4-1 is a block diagram
of the prototype device. The prototype device consists of a
unique parallel-plate ionization chamber that is connected
to a unique electrometer amplifier. The output of the
electrometer amplifier is feed to a computational unit which
performs inverse-square law computations. The output of the
computational unit is connected to a scaling circuit which
provides adjustments for unit calibration. Finally, a
digital voltmeter measures the output voltage of the scaling
circuit.

The prototype device is contained in three modules.
The first module consists of the ionization chamber, the
electrometer and the mounting brackets for collimator port
attachment. The second module or control module houses the
computational unit circuitry, the dual scaling circuitry,
the switching and resetting circuitry and the digital
voltmeter. The third module or power supply module houses
the power supplies. Shielded multiconductor cable with
multipin connectors link the modules together.
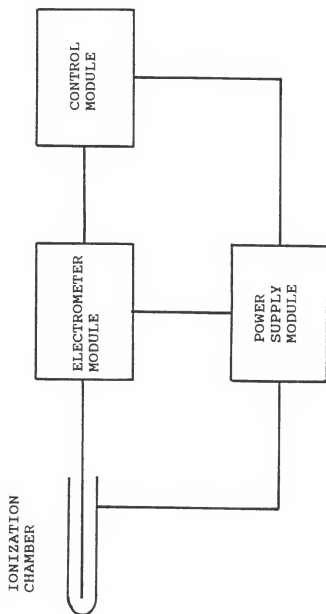
Figure 4-1: Block diagram of prototype device

Design of Ionization Chamber

The design of the prototype parallel-plate ionization chamber encompassed many different criteria. The main objectives of the design include the ability to be relatively transparent to visible light, to interact with photons in a manner similar to a practical ionization chamber, to be relatively homogeneous so that its shadow is not apparent on a image receptor and to have an active volume well defined and continuously in the primary beam during patient examinations.

Visible Light Transmission

Diagnostic radiographic x-ray machines and some fluoroscopic x-ray machines utilize a collimator light to help delineate the location of the x-ray field. The collimator light bulb is mounted in the interior of the collimator and outside the primary beam. A mirror is permanently mounted at an angle in the primary beam. The position of the light bulb and mirror are aligned in such a fashion that the border of the light field coincides with the border of the x-ray field within a given tolerance.

Diagnostic x-ray technologists utilize the collimator light to help delineate the position of the x-ray field during patient examinations. The intensity of the

collimator light must be sufficient to allow the technologists to discern the edges of the projected light under different ambient light conditions. Federal regulations state that when a light localizer is used to define the x-ray field, it shall provide an average illumination of not less than 160 lux at 100 cm or at the maximum SID, whichever is less (Code of Federal Regulations 1985).

Since the prototype ionization chamber covers the collimator port, the prototype ionization chamber will absorb and reflect a fraction of the visible light incident upon it. The fraction of visible light absorbed and reflected by the prototype ionization chamber depends on the materials utilized to construct the parallel-plates. The materials utilized to construct the parallel-plates were chosen to maximize visible light transmission while maintaining the characteristics necessary for a practical ionization chamber.

Polymethyl methacrylate (acrylic, lucite, plexiglass, perspex) was selected as a rigid base material for the parallel-plates. The percent visible light transmittances of acrylic, polycarbonate and glass utilizing the test method ASTM D1003, are 92, 89 and 89 respectively (Commercial Plastics and Supply Corporation; Richmond Hill, NY). The acrylic plates were coated with a thin layer of

silicon epoxy. The silicon epoxy coating was necessary to provide a suitable surface for adhesion of a conductive metal coating and to prevent out-gassing during the metal coating process.

The acrylic plates were then coated with a thin layer of indium tin oxide (ITO). A manufacturer specializing in transparent conductors stated that sputtered ITO had the highest visible light transmission of any conductive coating that was commercially available (Thin Film Device, Inc.; Anaheim, CA). Typical values of the percent visible light transmittance of sputter deposited ITO, gold and copper with a resistance of approximately 10 ohms per square on an optical grade polyester substrate are 87, 75 and 30 respectively (Andus; Canoga Park, CA).

Wall Thickness

In the standard free-air ionization chamber, the distance between each electrode plate and the sensitive volume of air must be larger than the maximum range of the electrons liberated by the photon interactions in air to ensure that the electrons expend all their energy before collection (Meredith and Massey 1977; Hendee 1984) and to ensure charged particle equilibrium (Ter-Pogossian 1967). The practical ionization chamber, in an analogous manner, replaces the relatively large thickness of air used in the

standard free-air ionization chamber with an air equivalent wall whose wall thickness is larger than the maximum range of the electrons liberated by the photon interactions in the wall.

The photon energies generally encountered in diagnostic radiology range from 10 to 120 keV. Infrequently, diagnostic modalities might employ a maximum photon energy of 150 keV. The maximum electron energy from an interaction with photons with the above energies would be 150 keV and the average electron energy would be significantly less. The substrate of the parallel-plates is acrylic.

Berger and Seltzer (1983) estimated the electron range (r_o) in different materials utilizing a continuous-slowing-down approximation in the following equation:

$$r_o = \int_{T_f}^{T_o} \frac{dT}{[S_{col}(T) + S_{rad}(T)]}$$

where T_o is the initial electron energy, T_f is the final electron energy, S_{col} is the collisional energy loss and S_{rad} is the radiative energy loss. The calculated continuous-slow-down approximation range of an 150 keV electron in acrylic is 2.894×10^{-2} g/cm^2. The density of acrylic is 1.190 g/cm^3. Thus the approximate range of an 150 keV electron in acrylic is 2.4×10^{-1} mm.

The acrylic substrate thickness should be approximately 2.4×10^{-1} mm or larger to ensure charged particle equilibrium. It was judged that an acrylic thickness of 1.5

mm was needed to maintain mechanical stability over a 170 mm x 200 mm sheet that was supported at its edges. The acrylic plate thickness of 1.5 mm also made machining processes easier and increased the plate resistance to mechanical breakage as compared with a thickness of 2.4×10^{-1} mm. Therefore, an acrylic substrate thickness of 1.5 mm was utilized to construct the parallel-plates.

Air-Equivalent Wall

The practical ionization chamber utilizes an air-equivalent wall. Ideally, an air-equivalent wall is composed of materials that have mass energy absorption coefficients identical to those of air. Although it is not possible to construct the ideal air-equivalent wall, nearly air-equivalent walls can be constructed. Two approaches are utilized to determine if compounds or mixtures have similar photon absorptions. The approaches utilized are the interaction data method and effective atomic number method.

White (1977b and 1978) discussed a tissue substitute simulation technique termed the basic data method which relied on the use of basic interaction data. For example the author states, if the photoelectric mass attenuation coefficient at a specific photon energy for a tissue $(\mu_\tau/\rho)_{tissue}$ is to be matched in a two component substitute, made up of a primary material A and a corrective filler B,

with corresponding photoelectric mass attenuation
coefficients $(\mu_\tau/\rho)_A$, $(\mu_\tau/\rho)_B$, the addition rule gives

$$(\mu_\tau/\rho)_{tissue} = \omega_A(\mu_\tau/\rho)_A + \omega_B(\mu_\tau/\rho)_B$$

where ω_A, ω_B are the proportions by weight of A and B in the
substitute. White also states that if the corrective filler
has been chosen carefully, this single estimate of the
proportions of A and B will give an acceptable simulation
over an extended energy range. The author concludes that
this method, which may be applied to both photon and
electron interactions, gives excellent results in practice,
but requires large quantities of interaction data for its
successful operation.

The photoelectric and incoherent (Compton) scattering
mass attenuation coefficients for air were calculated at
photon energies consisting of 10, 20, 30, 40, 50, 80 and 150
keV in Appendix A. A summary of the calculated interaction
coefficients is listed in Table 4-1. The photon
interactions of interest were those which were capable of
depositing energy at a photon energy range from 10 to 150
keV in a ionization chamber. For this reason, coherent
(Rayleigh) scattering and pair-production interactions were
not considered.

The wall of the prototype parallel-plate ionization
chamber consisted of an acrylic substrate that was coated
with silicon epoxy and indium tin oxide (ITO). The

radiation interaction properties of acrylic are similar to that of air. The thickness of the ITO coating was used to alter the photoelectric mass attenuation coefficients of the prototype ionization chamber. The radiation interaction properties of ITO include photoelectric absorption k-edges at 27.9 and 29.2 keV (Storm and Israel 1970). ITO photoelectric absorption k-edges are not present in the radiation properties of air and are thus undesirable.

TABLE 4-1
PHOTON INTERACTION COEFFICIENTS OF AIR

Photon Energy (keV)	μ_{incoh}/ρ (cm^2/g)	μ_{photo}/ρ (cm^2/g)
10	0.132	4.59
20	0.156	0.517
30	0.162	0.141
40	0.163	0.0556
50	0.161	0.0269
80	0.152	0.00581
150	0.132	0.000735

Several iterations using the interaction data method were necessary to determine that a ITO coating thickness of 2000 Angstroms per face was needed to increase the photoelectric mass attenuation coefficient of the prototype ionization wall to be approximately equivalent with that of air at 40 keV. The photoelectric mass attenuation

coefficient at 40 keV was selected as a equivalency reference point. Diagnostic radiology x-ray energy spectrums produced from a generator set between 60 and 120 kVp, have photon energies centered near 40 keV.

The photoelectric and incoherent scattering mass attenuation coefficients for a prototype parallel-plate ionization chamber were calculated at photon energies consisting of 10, 20, 30, 40, 50, 80 and 150 keV in Appendix B. A summary of the calculated interaction coefficients is listed in Table 4-2.

TABLE 4-2
PHOTON INTERACTION COEFFICIENTS
OF PROTOTYPE IONIZATION CHAMBER WALL

Photon Energy (keV)	μ_{incoh}/ρ (cm^2/g)	μ_{photo}/ρ (cm^2/g)
40	0.152	3.07
20	0.179	0.339
30	0.179	0.133
40	0.179	0.0554
50	0.176	0.0280
80	0.165	0.00664
150	0.143	0.000951

The wall of the prototype ionization chamber consisted of an acrylic substrate, a layer of silicon hardcoat and a layer of indium tin oxide (ITO) on each face. The thickness of the acrylic substrate was 1.49 mm. The thickness of the

silicon hardcoat layer was approximately 0.9 μm. The thickness of the ITO layer was approximately 2000 Angstroms. The manufacturer (Thin Film Device, Inc.; Anaheim, CA) which coated the acrylic substrate with the silicon hardcoat and ITO, provided information on the thickness of the coatings along with proprietary product information including chemical formulas, specific gravities and packing fractions.

In Figure 4-2, the calculated incoherent scattering mass attenuation coefficients of air and the prototype ionization chamber were plotted versus photon energy. The incoherent scattering mass attenuation coefficients of the prototype ionization chamber are slightly larger than those of air. In Table 4-3, the percent differences between the reference incoherent scattering attenuation coefficients of air and those of the prototype ionization chamber at specific photon energies are listed. A maximum difference of 15.8% was observed at 10 keV and a minimum difference of 8.35% was observed at 150 keV.

In Figure 4-3, the calculated photoelectric mass attenuation coefficients of air and the prototype ionization chamber were plotted versus photon energy. The photoelectric mass attenuation coefficients of air were larger than those of the prototype ionization chamber between 10 and 40 keV. The photoelectric mass attenuation
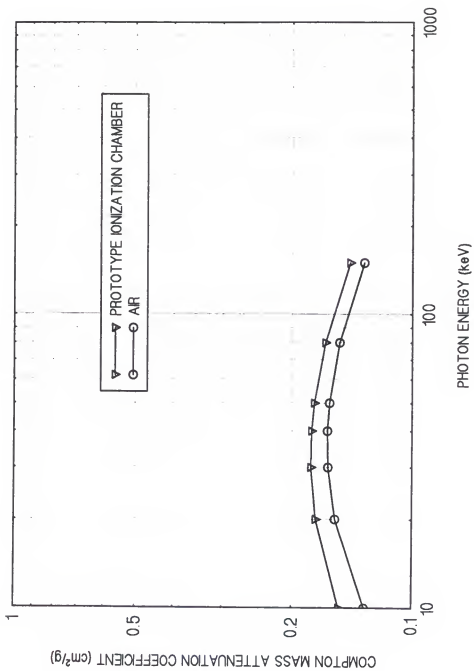
Figure 4-2: Comparison of Compton mass attenuation coefficients
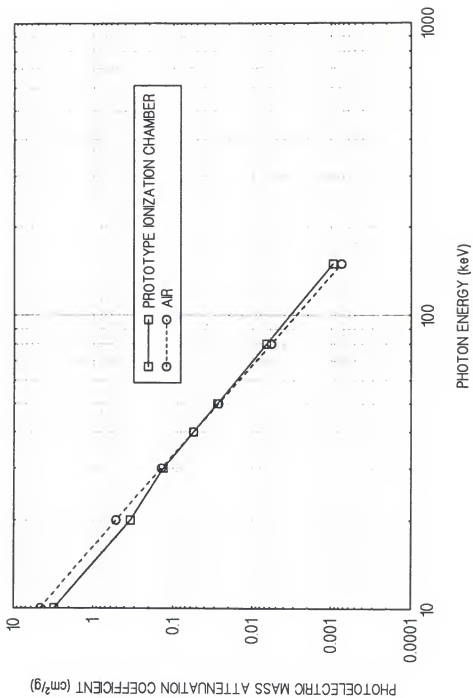
Figure 4-3: Comparison of photoelectric mass attenuation coefficients

coefficients of the prototype ionization chamber were larger than those of air for energies between 40 and 150 keV. In Table 4-3, the percent differences between the reference photoelectric mass attenuation coefficients of air and those of the prototype ionization chamber at specific photon energies are listed. At a photon energy of 40 keV, the calculated photoelectric mass attenuation coefficients of air and of the prototype ionization chamber were essentially equivalent.

TABLE 4-3
PERCENT DIFFERENCE BETWEEN THE PHOTON INTERACTION
COEFFICIENTS OF AIR AND PROTOTYPE IONIZATION CHAMBER WALL

Photon Energy (keV)	μ_{incoh}/ρ (%)	μ_{photo}/ρ (%)
40	15.8	−33.2
20	10.3	−34.5
30	10.3	−5.56
40	9.58	−0.412
50	9.19	4.08
80	8.44	14.3
150	8.35	29.5

Spiers (1946) used the concept of effective atomic number to calculate the effective atomic number of several chemical compounds which included C_5H_{12}, C_2H_3OH, H_2O, CO_2, MgO and NaCl. The author defined effective atomic number (Z_{eff}) as follows:

$$Z_{eff} = [\sum \alpha_i Z_i^{(m-1)}]^{(1/(m-1))}$$

where α_i is the fractional content of electrons belonging to each element, Z_i is the atomic number of the element and m is the exponent of Z which the photoelectric mass attenuation coefficient per atom is dependent upon. The author utilized 3.94 as the value of the exponent m in his calculations.

Spiers then plotted the experimentally determined mass attenuation per electron per gram of compound versus the compound effective atomic number raised to the power of 2.94. The observed linear relationship between mass attenuation per electron per gram and effective atomic number raised to the power (m-1) was used to assign effective atomic numbers to excised body tissues once the mass attenuation per electron per gram of body tissue was experimentally determined. Spiers noted that elements whose atomic number ranged from 1 to 5 displayed a different linear relationship between mass attenuation per electron per gram versus effective atomic number than did elements whose atomic number was greater than 5.

Weber and van den Berge (1969) employed the use of effective atomic number to calculate the composition of phantom materials. The authors plotted the log of the photoelectric cross section per atom (τ) versus the log of the atomic number (Z) for elements H, Be, N, O, Na, Mg, Al,

Si, P, S, Ar, K and Ca at specific energies and observed the following relationship:

$$\tau = kZ^m$$

where k is a constant and m is the exponent of Z that the photoelectric mass attenuation coefficient per atom is dependent upon. The authors calculated the exponent m by applying the least mean squares linear regression method to best fit the above equation at specific photon energies. For energies between 20 and 200 keV, the exponent m varied between 4.5 and 4.9. After omitting H and Be, the value 4.4 was chosen for the exponent m in order to give proper weight to the higher photoelectric absorption per atom at the lower photon energies. The authors stated that if the radiation quality was high, the exponent m may have been chosen a little high.

Weber and van den Berge then used the effective atomic number method in a manner similar to that of Spiers to calculate the composition of phantom materials with the exception that the value of the exponent m was changed from 3.94 to 4.4. Weber and van den Berge concluded that one can obtain an equivalent compound which has the same absorption and scattering properties as a given material within an accuracy of approximately 5 per cent using the effective atomic number method when the atomic numbers involved do not

exceed 20 and the energy range of interest is from 20 to 200 keV.

White (1977a) discussed the dependence of photon interactions upon atomic number. The author plotted the log of the photoelectric cross section (σ_a) versus the log of the atomic number (Z) for different groups of elements and at specific energies ranging from 10 to 150 keV and observed the following relationship:

$$\sigma_a = k(E)Z^m$$

where k is a constant and m is the exponent of Z that the photoelectric mass attenuation cross section per atom is dependent upon. The author calculated the exponent m by applying least mean squares linear regression method to best fit the above equation at specific photon energies. The values of the exponent m were averaged for each group of elements. Effective atomic numbers for compounds that were composed of elements from a specific grouping of elements were then calculated utilizing the average exponent m of the group.

White observed that as the photon energy was increased from 10 to 150 keV, the value of the exponent m increased and consequently the value of the calculated effective atomic number increased. The author concluded that the few published values of the exponent m are not adequate for

precise clinical radiation studies and that sets of values
of the exponent m yield more precise results.

As previously documented, the calculated effective
atomic number of a compound is related to the compound
photoelectric mass attenuation cross section. Although the
value for the exponent m varies as the photon energy and the
compound elements change, the calculated effective atomic
number can be a useful aid to evaluate if compounds or
mixtures have similar photoelectric absorptions.

Figure 4-4 shows the plot of the log of the
photoelectric mass attenuation cross sections versus the log
of the atomic number of nitrogen, oxygen and argon at a
photon energy of 40 keV. Nitrogen, oxygen and argon
contribute approximately 99.9 per cent to the total
photoelectric mass attenuation coefficient of air at 40 keV.
Therefore to obtain a representative value for the exponent
m, only those elements that contribute significant
photoelectric mass attenuation cross sections were employed
in the plot. The value of the exponent m was determined by
applying the least mean squares linear regression method to
best fit the equation

$$\tau = kZ^m$$

where τ is the photoelectric mass attenuation cross section,
k is a constant and m is the exponent of Z that the
photoelectric mass attenuation cross section is dependent
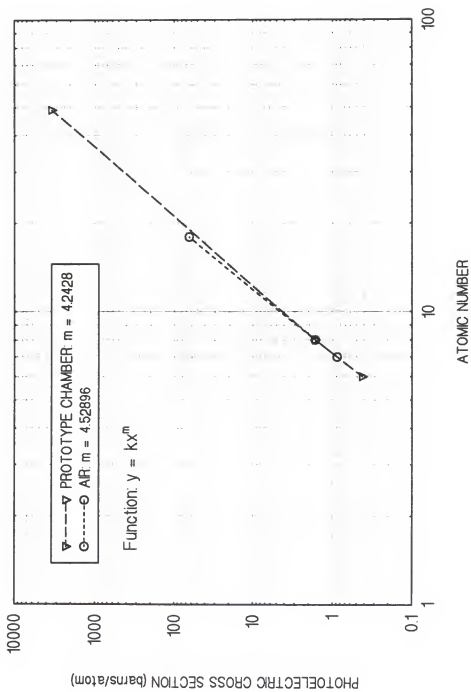
Figure 4-4: Dependence of photoelectric cross section on atomic number

upon. The value of the exponent m was determined to be 4.53. Appendix C contains a calculation of the effective atomic number of air at 40 keV utilizing 4.53 as the value of m. The calculated effective atomic number of air is 7.78.

Figure 4-4 also shows the plot of the log of the photoelectric mass attenuation cross sections versus the log of the atomic number of carbon, oxygen and indium at a photon energy of 40 keV. Carbon, oxygen and indium contribute approximately 95.8 per cent to the prototype parallel-plate ionization chamber's total photoelectric mass attenuation coefficient at 40 keV. Therefore to obtain a representative value for the exponent m, only those elements that contribute significant photoelectric mass attenuation cross sections were employed in the plot. The value of the exponent m was determined in a similar manner as that above. The value of the exponent was determined to be 4.24. Appendix D contains a calculation of the effective atomic number of the prototype ionization chamber at 40 keV utilizing 4.24 as the value of m. The calculated effective atomic number of the prototype ionization chamber is 7.66.

The calculated effective atomic number of air (7.78) is slightly higher than that of the prototype ionization chamber (7.66) at 40 keV. Thus the photoelectric mass attenuation coefficient of air at 40 keV should be slightly

larger than that of the prototype ionization chamber. The
photoelectric mass attenuation coefficient of air at 40 keV
is approximately 0.413% larger than that of the prototype
ionization chamber.

Physical Dimensions and Layout

Figure 4-5 is a diagram of the high voltage electrode
plate. The blackened areas of the diagram represent areas
of high electrical conductance resulting from the ITO
coating. The whitened areas represent areas of high
electrical resistance resulting from the removal the ITO
layer so that the silicon hardcoat or acrylic is exposed.
The central blackened area is the high voltage electrode.
The high voltage connection is accomplished by attaching a
metal connector to the finger projection of the central area
using silver epoxy (TRA-CON, Inc.; Medford, MA) and then
attaching the metal connector to a wire which is connected
to the high voltage source.

Figure 4-6 is a diagram of the collection electrode
plate. The blackened areas of the diagram represent areas
where the ITO coating is present. The whitened areas
represent areas where the ITO coating has been removed. The
central blackened area of the diagram resembling a lollypop
is the collection electrode. The collection electrode is
connected to the input of the electrometer amplifier. This

HIGH VOLTAGE ELECTRODE

Figure 4-5: Sketch of high voltage electrode plate
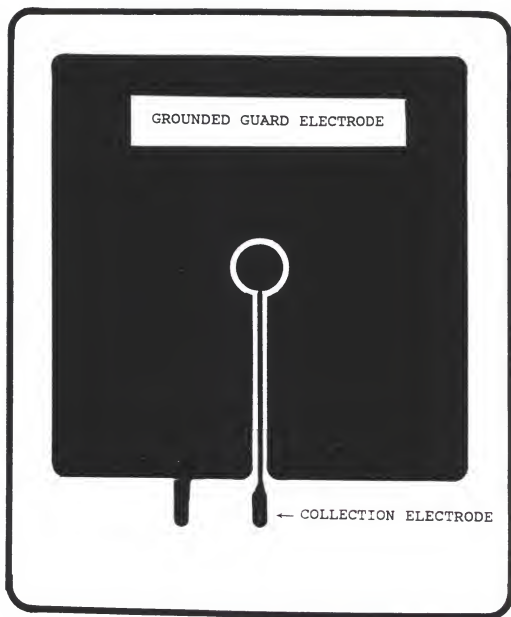
Figure 4-6: Sketch of collection electrode plate

connection is accomplished by attaching the central
conductor of a coaxial cable to the finger projection of the
central area using silver epoxy and then attaching the
central conductor of the coaxial cable to the input of the
electrometer amplifier. The blackened area immediately
surrounding the collection electrode is grounded. This
connection is accomplished by attaching a metal connector to
the finger projection of the surrounding area using silver
epoxy and then attaching the metal connector a wire which is
connected to ground potential.

Figure 4-7 is a diagram of the collection electrode
plate which has been modified. A part of the collection
electrode, the part that resembles the stick of the
lollypop, has been covered by a polyester film. The side of
the polyester film that may be in contact with the
collection electrode, has high electrical resistance. The
side of the polyester film that faces the high voltage
electrode, has high electrical conductance, resulting from
an ITO coating, and is grounded. The grounding was
accomplished by attaching the conductive side of the
polyester film to the grounded area surrounding the
collection electrode using silver epoxy. The polyester film
was physically attached to the grounded area surrounding the
collection electrode using adhesives.

GROUNDED OVERLAY COVERING
THE COLLECTION ELECTRODE STEM

Figure 4-7: Sketch of modified collection electrode plate

The other face of each plate is coated with ITO and is connected to ground potential. The grounded ITO plate faces function as a Faraday cage which shields its contents from radio frequency interference (RFI) and electromagnetic interference (EMI). The two electrode plates are separated by a aluminum spacer. The outer dimensions of the parallel-plate ionization chamber are approximately 17.0 cm x 20.0 cm x 0.88 cm. The sensitive volume of the prototype parallel-plate ionization has a cylindrical shape. The dimension of the radius at each end of the cylinder shaped sensitive volume is approximately 8.8 mm. The dimension of the sides of the cylinder shaped sensitive volume, which is equal to the parallel-plate separation distance, is approximately 5.2 mm. Therefore, the sensitive volume is approximately 1.3 cm^3.

Indium Tin Oxide Deposition and Etching

Eight 17.0 cm x 20.0 cm x 0.15 cm acrylic plates were coated on each face with a silicon hardcoat. The faces of the acrylic plates were then coated with indium tin oxide (ITO) using a proprietary sputter deposition process (Thin Film Device, Inc.; Anaheim, CA). The manufacturer coated the substrates with approximately 2000 Angstroms of ITO. The measured resistances of the eight plates ranged from 100 to 700 ohms per square. The varying resistances among the

plates strongly suggested that the thickness of the ITO layers also varied. The manufacturer would not provide any information on the correlation between ITO thickness and resistance per square. Thus the absolute thicknesses of the ITO layer on the substrates is not known.

The prototype parallel-plate ionization chamber design required that particular patterns of high electrical conductance and high electrical resistance be established on each plate. The particular patterns on the plates were established through the use of silk screen printing techniques and etching techniques.

The silk screen printing techniques utilized began with a creation of a life-sized pattern that showed the location of where the ITO was to remain. The pattern was then transferred to a stencil utilizing photographic techniques. The stencil was attached to a monofilament mesh (silk screen). The stencil was an impermeable membrane to the etch resist ink. The etch resist ink was squeezed through monofilament mesh in the areas that the stencil was not present. Two stencils were made. One stencil was for the high voltage electrode. The other stencil was for the collection electrode. Each plate had one face printed with a stencil and the other face was completely coated with the etch resist ink. The alkali soluble etch resist ink utilized was item 226 black (Naz-Dar/KC; Chicago, IL). The

etch resist ink was a resin based lacquer. The etch resist
ink was insoluble in various acid solutions. The etch
resist ink generally dried within a 24 hour period of time.

A solution containing 45% hydrochloric acid, 5% nitric
acid and 45% water by volume was poured into a glass
container that was large enough to submerge the item to be
etched. A printed plate was submerged in the acid solution
for approximately 1 minute to dissolve the ITO not covered
by the etch resist ink. The plate was then submerged in
several baths of distilled water to dilute any acid solution
remaining on the plate. A 2.44×10^{-2} molar sodium
hydroxide solution was poured into a clean glass container.
The etched plate was submerged in the alkali solution for no
longer than 10 minutes to dissolve the etch resist ink
located on both faces of the plate. The plate was then
submerged in several baths of distilled water to dilute any
alkali solution remaining on the plate.

Several problems were encountered utilizing the silk
screen printing techniques and etching techniques. Two of
the plates were destroyed because the silk screen printing
technician used a lacquer thinner that was incompatible with
the etch resist ink and the combination resulted in a ink
that could not be completely removed from the plates. Two
more of the plates were destroyed because the silk screen
printing technician attempted to remove wet ink from the

plates with an abrasive cloth which thoroughly scratched the
ITO coating. Apparently, some debris had been blown onto
the plates when the ink was in the process of drying. The
four plates that had the fewest artifacts in the ITO coating
upon delivery from the manufacturer, were the ones
destroyed.

The etching process and the handling of the plates left
some tiny scratches in the ITO coating. If the scratches
were long enough, the electrical continuity of a previously
continuous ITO coating could be broken. The collection
electrode thin strip of ITO that was described as the stick
of the lollypop, was very susceptible to a break its
electrical continuity. The silk screen and etching
processes seemed to enhance the artifacts already present
from the manufacturer deposition of the ITO coating.

Design of the Electrometer

The design of the electrometer encompassed many
different criteria. The main advantages of its design
included the short coaxial cable length from the collection
electrode to the input of the electrometer amplifier, the
relatively small leakage current at the input of the
electrometer amplifier, the small size of the electrometer
amplifier and its housing, the ability to calibrate the

electrometer for different x-ray tube locations relative to the x-ray table and the ability to measure exposure over a range from 1×10^{-3} to 1.999×10^3 Roentgen (R). The electrometer is primarily composed of three circuits consisting of the integration circuit, the electrometer reset circuit and the voltage invertor circuit. Figure 4-8 is a diagram of the electrometer circuits.

<u>Integration Circuit Design</u>

Figure 4-9 is a diagram of the integration circuit. The electrical analog of the mathematical integral operation can be obtained with the use of a operational amplifier and a feedback capacitor. The feedback capacitor is connected to both the inverting input and the output of the operational amplifier. Capacitance (C) is defined as

$$C \equiv Q/V$$

where Q is the electric charge and V is the voltage. Assuming the operational amplifier is ideal, then amplifier input resistance is infinite and the voltage between the amplifier inverting and noninverting inputs is zero. The input current (I) is

$$I = dQ/dt = C \, dV_o/dt$$

where V_o is the amplifier output voltage. Solving for dV_o and integrating, the equation becomes

RESET 1

RESET 2

VOLTAGE OUTPUT

86
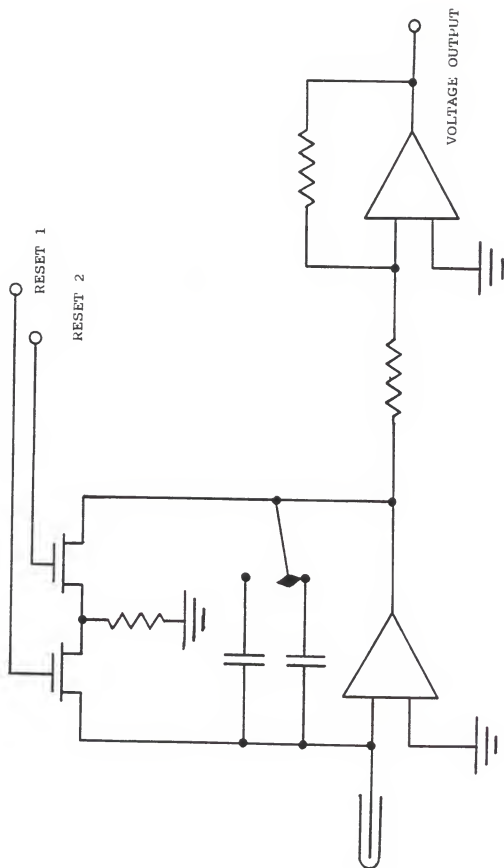
Figure 4-8: Circuit diagram of electrometer network
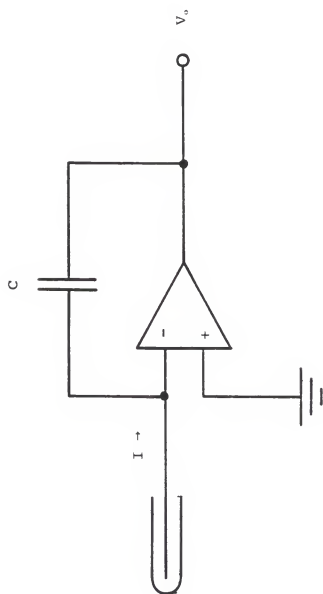
Figure 4-9: Circuit diagram of integration network

$$V_0 = \frac{1}{C} \int_0^t I dt$$

where t is the integration time.

Electrometer Reset Circuit Design

Figure 4-10 is a diagram of the integration circuit and the electrometer reset circuit. The electrometer reset circuit is mainly composed of two p-channel enhancement-mode metal oxide silicon field-effect transistors (MOSFET), a resistor and a momentary type mechanical switch. The transistors are normally nonconducting when their gate voltage is zero or positive. The transistors become conducting when their gate voltage falls below a negative threshold voltage. The feedback capacitor is electrically shorted or reset when the transistors are in a conducting phase. The feedback capacitor is in the integration or measurement mode of operation when the transistors are in a nonconductive phase. The conducting and nonconducting transistor phases are controlled by a mechanical switch which supplies either a negative voltage exceeding the gate threshold voltage or zero voltage to the transistor gates.

Practical ionization chambers produce small currents on the order of 10^{-12} to 10^{-9} ampere. Thus leakage current at the input of the operational amplifier must be minimized in order to reduce its contribution to a measurement. Two transistors are utilized to reduce the leakage current at
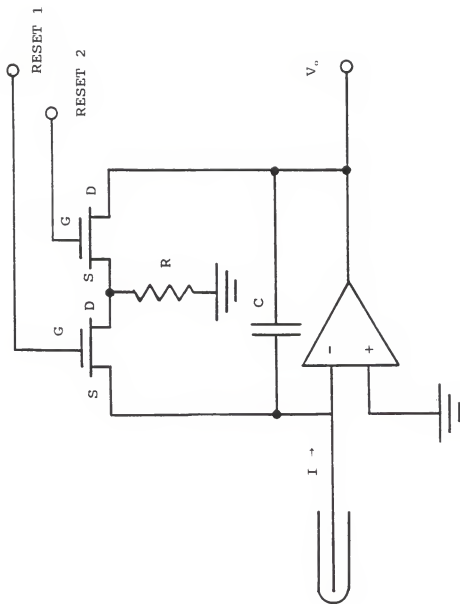
Figure 4-10: Circuit diagram of integration and reset networks

the input of the operational amplifier. The source of
transistor A is connected to the input of the operational
amplifier. The drain of transistor A is connected to the
source of transistor B and this electrical connection is
grounded through a small resistor. The drain of transistor
B is connected to the output of the operational amplifier.

A maximum voltage at the source of the transistor A can
be estimated. The voltage output of the operational
amplifier (V_o) is defined as

$$V_o \equiv - GV_e$$

where G is the open loop gain of the operational amplifier
and V_e is the voltage between the inverting and noninverting
inputs of the operational amplifier. Assuming $G = 10^5$ and
$V_o = -10$ volts, then $V_e = 10^{-4}$ volts. Since the source of
the transistor A is connected to the input of the
operational amplifier, the maximum voltage at the source of
transistor A is also on the order of 10^{-4} volts.

The gates of both transistors and the source and drain
of transistor A during integration or measurement mode of
operation are approximately at zero volts. Thus the
potential for leakage currents across transistor A during
the integration mode of operation is greatly reduced due to
the small voltage differences involved. Therefore,
utilizing two transistors effectively minimizes the leakage
current at the input of the operational amplifier.

In addition to two transistors and a momentary type mechanical switch, a dual precision monostable multivibrator and two resistor-capacitor (RC) networks are employed in the electrometer reset circuit. The dual multivibrator and the RC networks are utilized to provide stable sequences of voltages applied to the transistor gates. During the integration mode of operation, the mechanical switch, the two outputs of the multivibrator and the gates of the transistors are at approximately zero volts. The reset mode of operation is initiated when the momentary mechanical switch is activated. The mechanical switch momentarily supplies a negative voltage to the input of the dual multivibrator which activates its trigger. Once triggered, the voltages from the two multivibrator outputs change from zero to a negative value for a duration of time and then back to zero again. The length of the negative voltage pulse from each multivibrator is determined by the RC time constant for each circuit.

The RC time constant associated with the pulse that went to transistor A (0.98 s) is smaller than the RC time constant associated with the pulse that went to transistor B (1.0 s). Thus transistor B remains in a conducting or reset phase for a short period of time while transistor A is in a nonconducting or integrating phase. Figure 4-11 is a plot of the magnitude of the electrometer voltage offset upon
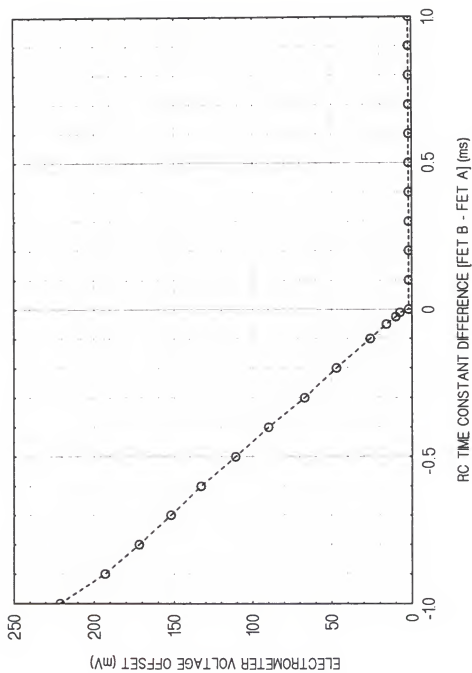
Figure 4-11: Dependence of voltage offset on FET reset timing sequences

reset versus the difference in the dual multivibrator RC
time constants. The RC time constants were measured with a
Hameg oscilloscope (referenced in Chapter 5).

The electrometer voltage offset remained relatively
small when the RC time constant associated with transistor A
was smaller than or equal to the RC time constant associated
with transistor B. When the RC time constant associated
with transistor A was larger than the RC time constant
associated with transistor B, the electrometer voltage
offset upon reset was significantly increased. Thus when a
two transistor amplifier reset network is employed, steps
must be taken to insure that transistor A is in a
nonconducting phase before transistor B finishes its
conducting phase upon reset.

The significantly increased electrometer offset voltage
upon reset when the RC time constant of the first transistor
exceeded that of the second transistor, was due to the
integration of a leakage current transferred from the gate
of transitor A to the the source of transitor A while
transitor A was in a conducting phase and transitor B was in
a nonconducting phase.

Electrometer Reset Circuit Analysis

An analysis of the electrometer reset circuit was
conducted to quantitatively assess the characteristics of

the network. Figure 4-12 is a diagram of circuit that is equivalent to the electrometer reset circuit. The amplifier input current (I), the amplifier input voltage V_i, the amplifier output voltage (V_o), the channel resistances of transistors A and B (R_1 and R_2), the resistance of the grounded resistor (R_3) and the voltage (V_j) at the junction of R_1, R_2 and R_3 are indicated in the diagram. Applying Kirchoff's law to the junction of R_1, R_2 and R_3, and assuming that the operational amplifier is ideal with a infinite input resistance, I is

$$I = - V_j/R_1 = (V_j - V_o)/R_2 + V_j/R_3.$$

Solving the equation for V_j, the equation becomes

$$V_j = V_o \frac{1}{1 + R_2/R_1 + R_2/R_3}.$$

Substituting for V_j, I is

$$I = - V_o \frac{1}{R_1 + R_2 + R_1R_2/R_3}.$$

Thus the apparent resistance (R_t) between the input and output of the operational amplifier is

$$R_t = R_1 + R_2 + R_1R_2/R_3.$$

Assuming that the channel resistance of each transistor is 10^{12} ohms when the transistors are in a nonconducting phase and R_3 is 500 ohms, then the apparent resistance between the input and output of the amplifier during the integration mode of operation is on the order of 2×10^{21} ohms. Thus utilizing two transistors in the amplifier reset circuit
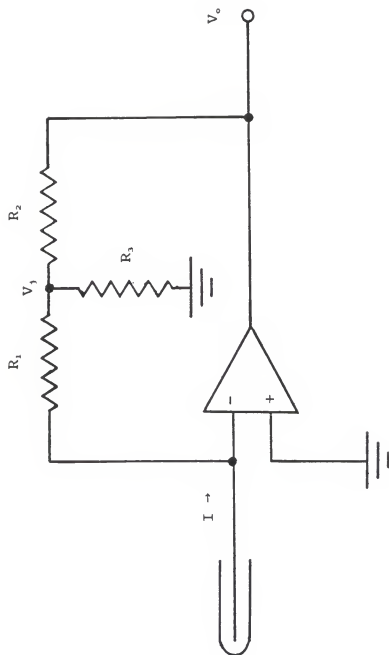
Figure 4-12: Circuit diagram of equivalent reset network

greatly increases the resistance between the operational amplifier input and output during integration as compared with utilizing a single transistor. Applying Kirchoff's law to the junction at the amplifier input in the above example, I is

$$I = -V_j/R_1 = -V_o/R_t.$$

Solving the equation for R_3, the equation becomes

$$R_3 = R_1 R_2 \frac{1}{(V_o/I) - R_1 - R_2}.$$

One characteristic of a properly designed electrometer reset circuit is that current through the reset network should be significantly less than the amplifier input bias current during integration. If the value of V_o/R_t is to be $1/10^6$ the value of the operational amplifier base current I when the nonconducting transistor channel resistances $R_1 = R_2 = 10^{12}$ ohms, $V_o = 10$ volts and $I = 40 \times 10^{-15}$ ampere, then the value of R_3 should be approximately 400 ohms.

Another characteristic of a properly designed electrometer reset circuit is that the RC time constant associated with the total resistance of the reset network and the capacity feedback capacitor C during the reset mode of operation should be much smaller than the reset network cycle time. This allows the operational amplifier output voltage to drop to zero, discharging the capacitor C before the completion of the reset cycle. If the conducting transistor channel resistances $R_1 = R_2 = 180$ ohms, $R_3 = 500$

ohms and C = 3 x 10^{-6} farad, then the RC time constant of
the reset network and the feedback capacitor is
approximately 1.3 ms. The durations of the conducting
phases of transistors are controlled by the RC time
constants of the externally added resistor-capacitor
networks of the dual multivibrators. The reset cycle time
is approximately 1.0 s. Thus the RC time constant
associated with the reset circuit and feedback capacitor is
much smaller the time of the reset cycle.

Voltage Invertor Design

Figure 4-13 is a diagram of the voltage invertor
circuit. The voltage invertor circuit is composed of a
input resistor R, a operational amplifier and a feedback
resistor R_f. The output of the electrometer amplifier is
connected to the inverting input of the invertor amplifier
through the resistor R. The amplifier input current is I,
the amplifier input voltage is V_i, the voltage between the
amplifier inverting and noninverting inputs is V_e, the
amplifier output voltage is V_o and the operational amplifier
open loop gain G = 10^5. Applying Kirchoff's law to the
amplifier input and assuming the operational amplifier is
ideal, then I is

$$I = (V_i - V_e)/R = (V_e - V_o)/R_f.$$

Since V_o is defined as
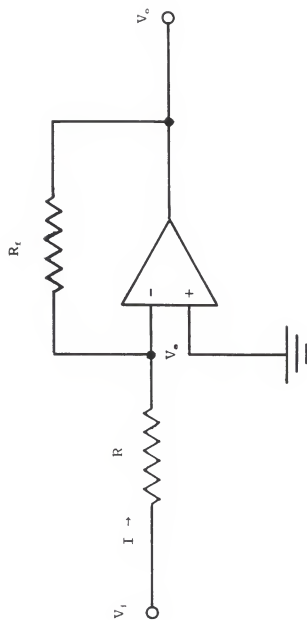
Figure 4-13: Circuit diagram of voltage invertor network

$$V_o \equiv -GV_e$$

and substituting for V_e, V_o is

$$V_o = -V_o/G - (R_f/R)(V_i + V_o/G).$$

Given $G = 10^5$ and V_o is a maximum of 10 volts, then $V_o/G \to 0$ and V_o is

$$V_o = - V_i(R_f/R).$$

Thus the voltage invertor circuit functions to reverse the polarity of the input voltage and to change the magnitude of the input voltage by a factor of R_f/R.

<u>Electrometer Components</u>

The operation amplifiers utilized in the integrating circuit and in the voltage invertor circuit were the AD549L (Analog Devices, Inc., Norwood, MA). This amplifier was chosen for its low input bias current of approximately 4 x 10^{-14} ampere, its low input offset voltage of approximately 0.3 mV and its high input impedance of approximately 10^{15} ohms. The open loop gain is approximately 10^5. The output voltage range is ± 12 volts and its operational temperature range is 0 to 70°C. The quiescent supply current is approximately 6 x 10^{-6} ampere. The AD549 was enclosed in a TO-99 hermetic package.

The two p-channel enhancement-mode MOSFETs utilized in the operational amplifier reset network were the 3N163 (Siliconix, Inc.; Santa Carla, CA) and were chosen for its

low leakage currents in the order of 10^{-11} ampere, its high nonconducting mode channel resistance of approximately 10^{12} ohms and its small input and output capacitances on the order of 10^{-12} farad. The transistors were enclosed in TO-72 packages.

The feedback capacitors utilized were of two different types. The 3600 pF capacitor was a polystyrene film capacitor and was selected for its high insulation resistance on the order of 10^{11} ohms, its low dielectric absorption of less than 0.02% and its good temperature stability and humidity protection. The 3.0 μF capacitor was a metalized polypropylene film capacitor was chosen for its relatively small size for its capacitance and its high insulation resistance.

The dual precision monostable multivibrator utilized was the CD4538BE type and was selected for its wide range of output pulse widths, its low quiescent current on the order of 10^{-6} ampere, its low transition times on the order of 10^{-7} s, its trigger stability and its flexibility for various applications. The multivibrator was enclosed in a 16-lead dual-in-line plastic package.

The mechanical switch utilized in the amplifier reset circuit was the 46 series (Grayhill; LaGrange, IL) single-pole double-throw break-before-make wiping contact switch. The switch is rated for 250,000 break and make operations.

The mechanical switch utilized to select between the two feedback capacitors was the 71 series (Grayhill; LaGrange, IL) single-pole single-throw 10 position adjustable stop rotary switch. The switch was chosen for its high insulation resistance on the order of 10^{10} ohms and its compact dimensions.

The electrometer circuit board was a fiberglass type with a copper overlay. Similar to the three other circuit boards in the prototype device, silk screen printing techniques were utilized in the manufacture of the circuit board patterns. The pattern of the circuit was first sketched and then pattern was photographically reduced to a specified size. The pattern was photographically transferred to a stencil and the stencil was attached to a monofilament mesh. Alkali removable etch resist ink was squeezed through the stencil openings and on to the circuit board to make the circuit patterns. Once the ink was dry, the board was placed in a acid solution to dissolve the areas of copper not covered by the etch resist ink. The board was removed from the acid solution and placed in a water bath to dilute any acid adhering to the board. The circuit board was placed in a weak alkaline bath to disolve the ink and then in a water bath to dilute any alkali adhering to the board. The board was dried. The board was

then drilled at designated sites to allow for insertion of the electrical components.

The site on the electrometer circuit board for the operation amplifier input was enlarged to accommodate a teflon press-mount terminal. The teflon terminal was used to isolate the amplifier input from the leakage currents on the fiberglass circuit board. The teflon terminal also provided a stable mount for the junction consisting of two capacitors, the coaxial cable center electrode, the source of transistor A and the operational amplifier input.

The coaxial cable used to connect the collection electrode of the ionization chamber to the input of the operational amplifier was RG type 196A/U. The coaxial cable was composed of a 30 gauge silver-coated copperweld center conductor, a 0.86 mm outer diameter tetrafluoroethylene (teflon) dielectric, a silver-coated copper shield with 95% coverage and a 1.9 mm outer diameter teflon tape jacket. The length of the coaxial cable was kept to a minimum of approximately 9 cm to reduce some the unwanted characteristics associated with coaxial cables. Spokas (1980) investigated several unwanted characteristics of ionization chamber cables including inherent noise currents, currents produced from cable movements, degree of shielding of the central conductor and radiation-induced cable currents. The author recommended that the center conductor

should be as fine as practical to reduce the magnitude of the radiation-induced current. Based on the test results, the author observed that the best performing cables had an inner dielectric insulation made of solid teflon. The RG type 196A/U coaxial cable has a relatively small gauge center conductor and the inner dielectric is solid teflon.

The electrometer is housed in a aluminum enclosure. The enclosure is grounded and functions as a Faraday cage which shields its contents from radio frequency interference (RFI) and electromagnetic interference (EMI).

Design of Control Module

The control module consists of two linear potentiometer networks, a real-time analog computational unit, two scaling circuits, a digital voltmeter and a mechanical switch. Figure 4-14 is a diagram of the control module circuits.

Potentiometer Network Design

Two identical potentiometer networks are utilized. The purpose of the potentiometer networks is to supply two voltages to the computational unit that are proportional to specific distances. One potentiometer network supplies a voltage that is proportional to the source-to-detector distance (SDD). The detector measurement point is midway
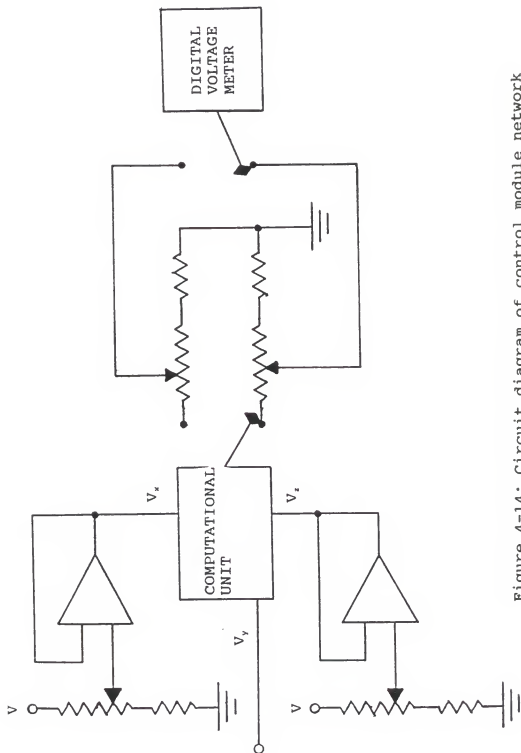
Figure 4-14: Circuit diagram of control module network

between the parallel-plates of the prototype ionization chamber. The other potentiometer network supplies a voltage that is proportional to the source-to-skin distance (SSD). The operator of the ionization chamber measures both the SDD and the SSD and rotates the turns-counting dials of the potentiometers to the appropriate positions calibrated in centimeters. The potentiometer network output voltage increases with increasing dial number or distance.

Figure 4-15 is a diagram of one of the two identical potentiometer networks. A potentiometer network is mainly composed of a precision potentiometer with counting dial, a operational amplifier, a resistor and a voltage source. A voltage source is connected to the potentiometer clock-wise (CW) terminal. The potentiometer counter-clock-wise (CCW) terminal is grounded. The potentiometer wiper or slider is connected to the noninverting input of the operational amplifier. The output of the operational amplifier is connected to a computation unit through a resistor. The resistance of the potentiometer is R. The resistance between the slider and the CCW terminal is fR where f is the remaining fraction of the total potentiometer resistance between CCW and ground. The resistance between the CW terminal and the slider is $(1-f)R$. The resistance of the resistor at the input of the computation unit is R_1. The
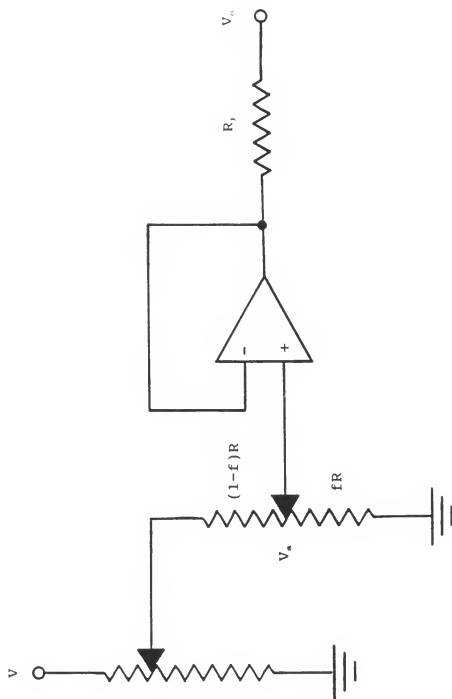
Figure 4-15: Circuit diagram of potentiometer network

voltage source is V and the voltage at the potentiometer slider is V_s.

The operational amplifier connected in this manner functions as a noninverting voltage follower where the amplifier output voltage is the same phase and magnitude as the input. Applying Kirchoff's law and given the operational amplifier input impedance is on the order of 10^{12} ohms, V_s is

$$V_s = fV.$$

Given $R = 5 \times 10^3$ ohms, $R_1 = 2.5 \times 10^4$ ohms, $f = 0.5$ and $V = 15$ volts, then $V_s = 7.5$ volts and R_1 does not effect the voltage linearity of the network.

In the above example, if the operational amplifier were removed from the circuit and the potentiometer slider was connected in series with R_1, applying Kirchhoff's law at the slider V_s is

$$V_s = VR_p/R_t$$

where $R_p = [fRR_1/(fR + R_1)]$ and $R_t = (1-f)R+R_p$. Substituting in for the given values, $V_s = 7.1429$ volts. If $f = 0.25$ and the other given values remain the same, $V_s = 3.6145$ volts. As the f value increased by a factor 2, the V_s value increased by factor of less than 2. Thus, the circuit without the operational amplifier is not linear and this is due to the influence of R_1 loading down the voltage of the potentiometer network.

The turns-counting dials were calibrated to the potentiometers using a multimeter to measure the resistances of the potentiometers at multiple turns. A small resistance trimming potentiometer and a 1% tolerance resistor were attached to each network between the voltage source and the precision potentiometer CW terminal. The trimming potentiometers and fixed resistors were utilized to decrease the wiper voltages from 15 to 10.00 volts when the wipers were at the CW terminals. The specifications for the computational unit stated that its input voltages could not exceed 10 volts.

Computational Unit Design

The electrometer output voltage is directly proportional to the exposure measured at the SDD location. Since the SSD and SSD are different, an inverse-square distance correction must be made in order for the voltage to be directly proportional to entrance skin exposure free-in-air (ESE). A analog computational unit is utilized to alter the magnitude of the electrometer output voltage so that the computational unit output voltage is directly proportional to ESE. The computational unit conducts a series of mathematical operations according to the following equation:

$$V_o = V_y \, (V_z/V_x)^m$$

where V_o is the output voltage, V_y, V_z and V_x are input voltages and the exponent m is determined by the magnitude of externally added resistance at a specific location. V_y is the electrometer output voltage. V_z is the potentiometer network output voltage that is proportional to the SDD and V_x is the other potentiometer network voltage that is proportional to the SSD. The exponent m is equal to two when the externally added resistance between pins 17 and 18 on the computational unit is 196 ohms.

Scaling Network and Readout Design

The purpose of the scaling network is to reduce the computational unit output voltage so that the resultant voltage is proportional to a unit of measurement desired. The unit of measurement selected for the prototype device is the Roentgen. Two scaling networks were employed and a mechanical switch enabled the user to select the appropriate network. One scaling network was to be used when the smaller electrometer feedback capacitor was selected and the other scaling network was to be used when the larger electrometer feedback capacitor was selected. Therefore, the mechanical switches in the both the electrometer feedback capacitor circuit and the scaling circuits must be in the appropriate setting for proper function.

Figure 4-16 is a circuit diagram of a scaling network. The computational unit output voltage is connected to a double-pole double-throw mechanical switch. One mechanical switch throw is connected to a trimming potentiometer (R) terminal end. The other potentiometer terminal end is connected to ground through a resistor (R_1). The potentiometer wiper is connected to the another mechanical switch throw. The other mechanical switch pole is connected to the digital voltage meter. Since the voltage meter input impedance (R_2) is approximately 10^9 ohms, the wiper voltage is directly proportional to the voltage meter reading. The resistances of the resistors in the scaling networks were selected so that the range and precision of the scaling allowed proper adjustment to the unit desired and so that the computational unit output amplifier was not loaded down.

The output of the scaling network is connected in series with a digital voltmeter. The 4 1/2 digit liquid crystal display of the voltmeter serves as the readout. The control module is housed in a aluminum enclosure. The enclosure is grounded and functions as a Faraday cage which shields its contents from RFI and EMI.

Control Module Components

The two precision potentiometers utilized in the potentiometer networks were the 533 wirewound model
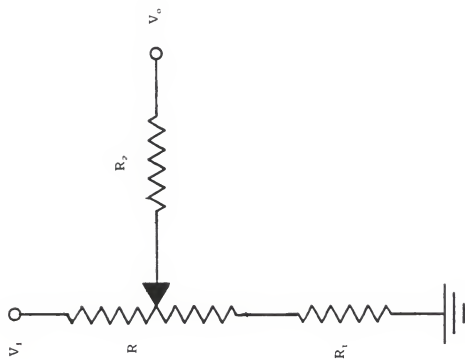
Figure 4-16: Circuit diagram of scaling network

(Spectrol; Ontario, CA). This potentiometer was chosen for its 3-turns, its ± 0.25% linearity, its ± 5% resistance tolerance, its power rating of 1.5 watts, its temperature operating range from -55 to 125°C, its rotational life on the order of 3×10^5 revolutions and its 0.25 inch diameter shaft. The turns-counting dials that were attached to the shafts of the potentiometers were the CT26 models (Bourns, Inc.; Ogden, UT). This model was chosen for its 10-turn range, its readability to within 0.002 of a turn, its white-on-black background markings, its acceptance of a 0.25 inch shaft diameter and its positive friction locking brake.

The trimming potentiometers in the potentiometer networks were the 3006P type. The trimming potentiometer was chosen for its 15-turns, its resistance tolerance of ± 10%, its power rating of 0.75 watt and its low resistance range availability.

The two operational amplifiers utilized in the potentiometer networks were the CA3140B type. This amplifier was chosen for its high input impedance of approximately 10^{12} ohms, its low input bias current of approximately 10^{-11} ampere, its input offset voltage of approximately 2 mV, its rugged input stage and its relatively low cost.

The mechanical switch utilized in the potentiometer and scaling networks was a double-pole double-throw on/on panel

mount rocker type. The switch was rated for 16 amperes at 125 volts AC.

The real-time analog computational unit utilized was the AD538BD (Analog Devices, Inc.; Norwood, MA). The unit was chosen for its ability to preform precision analog multiplication, division and exponentiation, its resistor-programmable exponentiation, its low input and output offset voltages, its excellent linearity and its wide input an output dynamic range.

The trimming potentiometers in the scaling networks were the 3059Y type. The trimming potentiometer was chosen for its 22-turns, its power rating of 1 watt, and its resistance tolerance of ± 10%.

The digital voltmeter utilized as a readout device was the DP2000 model (Acculex; Taunton, MA). The voltmeter was chosen for its 4 1/2 digit liquid crystal display, its 10 mm numerical height display, its low power consumption on the order of 17 milliwatts, its choice of decimal point placement, its excellent accuracy of approximately 0.06% and its relatively small size and low cost.

The aluminum enclosure utilized to house the control unit was the TECH-BOX model (Extrusion Technology, Inc.; Randolf, MA). The enclosure was chosen for its aluminum case and panels, its integral RFI and EMI shielding, its built in heat sink, its corrosion resistance, its screw

tubes for quick panel installation, its custom grooves and bevels and its integral strength.

Design of the Power Supply Module and Module Interconnections

The power supply module consists of a power entry module, a 10 volt power supply, a direct current (DC) to DC converter, a triple power supply consisting of 5 and ± 15 volts and a large resistor and capacitor network. The power entry module contained a alternating current (AC) male connector, a radio frequency interference (RFI) filter, a fuse circuit and a on/off switch. A fast-acting 1.0 ampere fuse was utilized and the fuse amperage was based on a calculation combining the power supplies maximum power outputs, the power supplies AC-DC conversion efficiencies and a safety factor of eight.

The 10 volt power supply output was connected to the DC to DC converter. The DC to DC converter output voltage follows the input voltage with a gain by a factor of 50. Thus the converter output voltage is approximately 500 volts. The converter output voltage is connected in series with a 1×10^6 ohm resistor which is then connected to the prototype ionization chamber high voltage electrode. One end of a 1×10^{-6} farad capacitor is connected to the high voltage electrode and the other end is shunted to ground.

The RC network functions as a smoothing filter. The RC time constant is approximately 1 second which should be long enough to moderate any 60 hertz ripple from the converter voltage output.

The triple power supply provides the power to the circuitry. The 5 volt supply is the power source for the voltmeter. The 15 volt supply is a power source for the control module two potentiometer networks, the four operational amplifiers and the control module computational unit. The negative 15 volt supply is a power source for the four operational amplifiers, the two MOSFETs in the electrometer reset circuit, and the control module computational unit.

The power supplies are housed in a aluminum enclosure. The enclosure is grounded and functions as a Faraday cage which shields its contents from RFI and EMI. The module interconnections are accomplished through the use of shielded male and female locking circular connectors and shielded multiconductor cable.

Power Supply and Interconnection Components

The 10 volt linear encapsulated power supply was the P33-10ST model (Polytron Devices, Inc.; Paterson, NJ). The power supply was chosen for its line regulation of 0.1%, its load regulation of 0.1%, its root-mean-square (RMS) ripple

and noise of 1.0 mV, its voltage output tolerance of ± 1%, its maximum output current of 150 mA and its operating temperature range from - 25 to 71°C.

The triple voltage linear encapsulated power supply was the P52-15T model (Polytron Devices, Inc.; Paterson, NJ). The power supply was chosen for its line regulation of 0.02%, its load regulation of 0.1%, its RMS ripple and noise of 1.0 mV, its voltage output tolerance of ± 1%, its maximum output current of 250 mA for the 5 volt source and ± 100 mA for the ± 15 volt source and its operating temperature range from -25 to 71°C.

The fully encapsulated DC to DC converter was the D500 model (Emco High Voltage Company; Sutter Creek, CA). The converter was chosen for its floating input/output voltage, its load regulation of 5%, its line regulation which follows the input, its peak-to-peak output ripple of 0.5% and its operating temperature range from - 10 to 60°C.

The aluminum enclosure utilized to house the power supplies was the TECH-BOX model (Extrusion Technology, Inc.; Randolf, MA). The enclosure was chosen for its aluminum case and panels, its integral RFI and EMI shielding, its built in heat sink, its corrosion resistance, its screw tubes for quick panel installation, its custom grooves and bevels and its integral strength.

The male and female circular connectors utilized were the SV 70, the KV 70, the SFV 70 and KFV 70 models (Lumberg Inc.; Richmond, VA). The connectors were selected for their effective test voltage rating of 2000 volts, their contact insulation resistance of approximately 10^{13} ohms, their compact design, their metal screw locking mechanism and their solder-type mode of connection.

The multiconductor cable utilized was the 9612 type. The cable was selected for its seven 24 gauge tinned copper conductors, its aluminum foil shield, its tinned copper braid shield and its polyvinyl chloride (PVC) insulation and jacket and its low capacitance of 3×10^{-11} farad per foot.

CHAPTER 5
EVALUATION AND DISCUSSION OF THE PROTOTYPE DEVICE

The evaluation of the prototype device covered two areas which consisted of electronic characteristics and characteristics upon irradiation. The equipment used during the evaluation of the prototype device included noninvasive test equipment, invasive test equipment and x-ray generating equipment.

The noninvasive test equipment utilized included a photometer, an exposure meter or dosimeter, a densitometer, a thermometer and a barometer. A calibrated UDT model S351C-LP (United Detector Technology; Hawthorne, CA) photometer was used to measure illuminance in units of lux. The accuracy of the photometer calibration was ± 3%. A calibrated Radcal model 1015 radiation monitor and model 10X5-6 ionization chamber (Radcal Corporation; Monrovia, CA) was used as a reference dosimeter. A new high voltage battery was utilized and its voltage did not fall below 300 volts during the evaluation of the prototype device, meeting Radcal specifications. The accuracy of the dosimeter calibration was ± 5%. A calibrated X-Rite model 301 (X-Rite, Inc.; Grandville, MI) densitometer was used to measure the optical density of radiographs. The accuracy of the

densitometer calibration was ± 0.020. A calibrated Nuclear
Associates model 07-402 (Nuclear Associates, Division of
Victoreen, Inc.; Carle Place, NY) portable digital
thermometer was used to measure ambient temperatures. The
accuracy of the temperature calibration was ± 0.2°C. A
calibrated barometer located in the United States National
Weather Service Station at the Gainesville Regional Airport
(Gainesville, FL) was used to measure barometric pressure.
The accuracy of the barometric pressure calibration was ±
0.001 inches of mercury.

The invasive test equipment utilized included a
multimeter, an oscilloscope, a voltage divider and a DC
voltage source. A calibrated Fluke model 27 (John Fluke
Manufacturing Company, Inc.; Burbank, CA) digital multimeter
was used to measure voltage and resistance. The accuracy of
the voltage calibration was ± 0.1% and the resistance
calibration was ± 0.2% to ± 1.0%. A calibrated Hameg model
HM 205-2 (Hameg; Port Washington, NY) dual channel digital
storage oscilloscope was used to measure the pulse height
and width of input signals. The accuracy of the voltage
calibration was ± 3% and the time calibration was ± 3%. A
calibrated Machlett Dynalyzer II high voltage unit and
digital display (Machlett Laboratories, Inc.; Stamford, CT)
was used to measure the x-ray tube peak kilovoltage
potential (kVp). The calibration kVp accuracy of the

Dynalyzer was ± 1%. An Ortec model 456 (EG&G Ortec; Oak Ridge, TN) variable precision DC voltage source was used as a voltage power supply. The smallest graduation on the turns-dial counter of the power supply was 0.2 volt.

The x-ray equipment utilized for testing purposes included a radiographic unit and a radiographic and fluoroscopic unit. A Philips equipped radiographic unit (Philips Medical Systems, Inc.; Shelton, CT) with a Maximus C850 three-phase twelve-pulse generator was utilized. A Siemens equipped radiographic and fluoroscopic unit (Siemens Medical Systems, Inc.; Concord, CA) with a Polydoros 80S high frequency generator was utilized.

Electronic Characteristics

An evaluation of several prototype device electronic characteristics was conducted. The characteristics evaluated consisted of the electrical resistance of the etched ITO plates, the leakage current associated with the electrometer input and the linearity error associated with the inverse square computational network.

Etched Indium Tin Oxide Plates

As stated in Chapter 4, the etching processes and handling of the plates left some tiny scratches in the ITO

coating. The etching processes seemed to enhance the defects created at the time of manufacture. If the defects were deep enough to completely penetrate the ITO coating and long enough to isolate any particular area, a previously continuous ITO coated area would not be continuous. The severity of consequence from an unplanned break in the ITO coating would depend on the specific area affected and the area function.

The two etched plates of the parallel-plate ionization chamber were evaluated for unplanned breaks in the ITO coating. Measurements of electrical resistance between areas of the ITO coating that were planned to be continuous and had important function were documented. A Fluke multimeter was used to measure resistance. The maximum resistance measurement of the multimeter was 32×10^6 ohms. The high voltage electrode had a resistance on the order of 10^3 ohms between its connector and its other areas. The collection electrode had a resistance greater than 32×10^6 ohms between its connector and its lollypop shaped area. The grounded area surrounding the collection electrode had a resistance on the order of 10^3 ohms between its connector and its other areas. The ionization chamber two outer faces had resistances on the order of 10^4 to greater than 32×10^6 ohms between their different areas.

The collection electrode had a scratch across its stick shaped area and that scratch broke the electrical continuity of the collection electrode. A graphite containing compound was sprayed over the stick shaped area of the collection electrode to make the collection electrode electrically continuous. The graphite sprayed collection electrode had a resistance on the order of 10^3 ohms between its connector and its lollypop shaped area. The ionization chamber two outer faces had areas of significant defects in the ITO coating located more towards the edges. The two outer faces of the ionization chamber had few defects in the center portion of their areas which were located over the sensitive volume of the ionization chamber.

Leakage Current at Electrometer Input

The leakage current at the input of the electrometer amplifier is the sum of the leakage currents from the ionization chamber, the coaxial cable, the electrometer operational amplifier, the feedback capacitors, the reset network, the mechanical switch and the teflon terminal. The leakage current at the electrometer input was measured in the following manner.

The turns-dial counters of both control module potentiometer networks were positioned at 100.0 cm. The electrometer mechanical switch was positioned to select the

3.6 x 10^{-9} farad feedback capacitor. The electrometer aluminum cover plate was removed. A 8.9 x 10^{10} ohm resistor was connected to the positive terminal of a 9 volt battery and the negative battery terminal was connected to the electrometer common or ground. The resistor lead not connected to the battery was placed in contact with the input of the electrometer which charged the feedback capacitor. The charging circuit was removed when the control module voltmeter was near a maximum reading. The aluminum cover plate was fastened to the electrometer and the prototype device was allowed to stabilize for a few minutes before a measurement was begun.

The control module voltage measurement was documented at the same moment that a stop watch was activated. After a period of time to allow a significant change in the voltage measurement value, a voltage measurement was documented along with the associated time period. The leakage current (I) was calculated using

$$I = dQ/dt = C \, dV/dt$$

where C is the capacitance of the feedback capacitor in farad, dV is the change in the voltage measurement values in volts and dt is the change in the time measurements in seconds. The leakage current at the electrometer input was 9 x 10^{-15} ampere.

Waggener (et al. 1982) stated that a Farmer-type ionization chamber typically has a leakage current in the order 10^{-13} ampere. The authors also stated that the leakage current must be small compared to the useful signal during exposure and suggested 0.1% as a maximum. The specified leakage current for the diagnostic electrometer RMI DD-1 model (Gammex RMI; Middleton, WI) without an attached ionization is less than 8 x 10^{-14} ampere. Certainly, leakage current at the input of an electrometer should be minimized.

The prototype device leakage current at the electrometer input is approximately a factor of 10 less than that stated for the typical Farmer-type chamber and similar to that specified for the diagnostic electrometer without an attached ionization chamber. The prototype device electrometer leakage current could be further reduced by filling the electrometer aluminum housing with ceresin wax. Ceresin wax is an excellent insulator and would eliminate the electrometer leakage currents caused by humidity effects. Ceresin wax utilization would also reduce the affect of the electrometer input functioning as a small ionization chamber during irradiation and would reduce the noise resulting from microphonic affects created through mechanical vibration. The prototype device relatively small leakage current is acceptable for its stated purposes.

Inverse Square Computational Network

The linearity errors associated with the control module potentiometer networks and computational unit were evaluated. A charge was placed on the feedback capacitor which resulted in a electrometer output voltage V_y. The two potentiometer network output voltages V_z and V_x were varied in different steps. V_z is proportional to the SDD and V_x is proportional to the SSD. The resultant computational unit output voltage was measured by a Fluke multimeter to within three significant figures.

The observed measurement at the SSD at 100.0 cm was used as a reference point in all the percent error calculations. Percent error was defined as

$$\% \text{ Error} = \frac{[\text{Expected} - \text{Observed}]}{\text{Expected}} \, 100\%.$$

The expected value was derived from applying an independent inverse-square distance correction calculation to the reference point value at the selected SDD and SSD. The observed value was the measured computational unit output voltage V_y. The effect of the electrometer leakage current on the electrometer output voltage value was negligible during the relatively short durations of time required for each group of measurements.

Figure 5-1 is a plot of the calculated percent errors versus the SSDs at five different SDDs. The five SDDs
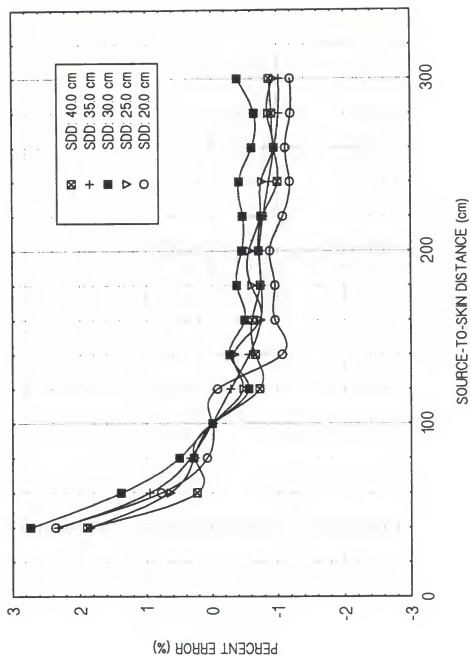
Figure 5-1: Inverse square percent error at different source-to-detector distances

utilized in the plot were 20.0, 25.0, 30.0, 35.0 and 40.0
cm. The SDDs ranging from 20 to 40 cm should encompass most
prototype ionization chamber installations. The SSDs
clinically used, range from approximately 60 to 180 cm. The
percent errors associated with the clinically used SDDs were
approximately ± 1%. A ± 1 percent error over the range of
clinically used SDDs and SSDs for the potentiometer networks
and the computational unit is relatively low especially
after considering that the smallest graduation mark on the
turns-dial counters is 0.2 cm. A ± 1 percent error is
acceptable for this analog circuitry.

Characteristics Upon Irradiation

An evaluation of the prototype device characteristics
upon irradiation was conducted. The characteristics
evaluated consisted of the visible light transmittance, the
aluminum equivalent, the energy rate dependence and bias
voltage selection, the capacitor selection and calibration,
the linearity dependence, the energy dependence, the x-ray
field size dependence, the stem dependence and the patient
backscatter dependence.

Visible Light Transmittance

As stated in Chapter 4, the materials utilized to construct the prototype parallel-plate ionization chamber were chosen to maximize visible light transmission while maintaining the characteristics necessary for a practical ionization chamber. The prototype ionization chamber visible light transmittance was measured in the following manner.

The collimator light illuminance was measured with an UDT photometer at a distance of 100 cm between the source and the photometer detector. The light field size at a SDD of 100 cm was approximately 45 cm x 45 cm. The center of each quadrant of the light field was marked. Ambient light was reduced by turning-off the overhead room lights. Four measurements of the collimator light illuminance were taken at the marked positions in each quadrant. The prototype ionization chamber was then mounted to the bottom of the collimator, completely covering the collimator port. Four measurements of the collimator light illuminance were taken at the marked positions in each quadrant. The background light was measured at the marked positions in each quadrant. The average collimator illuminance without the ionization chamber in the light field was called I_1. The average collimator illuminance with the ionization chamber in the light field was called I_2. The average background light

value was called B. The prototype ionization chamber
visible light transmittance was calculated using the formula

$$\% \text{ Transmittance} = 100\% \ (I_2 - B)/(I_1 - B).$$

The visible light transmittance of the prototype
ionization chamber was 49%. If the collimator light
illuminance without the ionization chamber in the light
field is greater than 326 lux, then the collimator
illuminance with the ionization chamber in the light field
would meet the Federal regulatory requirements of providing
an average illumination of not less than 160 lux (Codes of
the Federal Register 1985). The collimator light
illuminance without the ionization chamber placed in the
light field was 346 lux. If the collimator light
illuminance falls below the regulatory limit, the x-ray
technologist may have difficulty in delineating the position
of the light field and the congruent x-ray field during
patient examinations.

Aluminum Equivalent

The aluminum equivalent of the prototype ionization
chamber was evaluated with the use of test equipment which
included a Philips radiographic unit, a Radcal dosimeter, a
Machlett Dynalyzer, a test stand, a selection of different
thickness 1100 alloy aluminum filters and a lead plate with
aperture. The generator technique factors were adjusted to

produce a Dynalyzer measurement of 100 kVp. The Radcal ionization chamber was attached to the test stand and the stand was positioned so that the SDD was 90 cm and the nearest backscatter substrate was 290 cm away from the dosimeter. A lead plate with a 10 cm x 10 cm aperture was placed in the filter slot of the stand and the x-ray field was centered to the aperture. The x-ray tube collimator was adjusted so that the x-ray field size at the aperture of the lead plate was 8 cm x 8 cm.

The generator control panel technique factors were not changed during the aluminum equivalent measurements. A series of four exposures were measured for each aluminum filtration thickness placed on top the aperture of the lead plate. Before and after a group of three filtration thicknesses were measured, a series of four exposures were measured with no filtration over the aperture of the lead plate. This procedure monitored the consistency of the generator output. Eight aluminum filter thicknesses were exposed in addition to the prototype ionization chamber.

Figure 5-2 is a plot of the added aluminum filtration thickness versus the relative exposure. The relative exposure was calculated by dividing the averaged exposure measurement of a aluminum filtration thickness by the averaged exposure measurement with no filter present. The x-ray beam quality was characterized by a first half-value
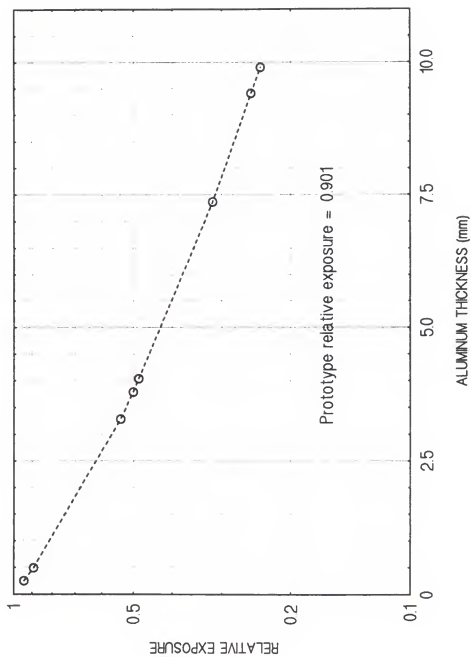
Figure 5-2: Aluminum equivalent of prototype ionization chamber

layer (HVL) of 3.78 mm of aluminum and a second HVL of 5.72 mm of aluminum at a x-ray tube potential of 100 kVp. The aluminum equivalent of the prototype ionization chamber was determined by calculating its relative exposure and then using the plot to locate the aluminum filtration thickness associated with its relative exposure. The aluminum equivalent of the prototype ionization chamber was 0.46 mm.

Ideally, the aluminum equivalent of the prototype ionization chamber should be zero to minimize its photon attenuation. If the photon attenuation of the prototype ionization chamber is significant, the x-ray technologist would have to increase the x-ray generator technique factors in order to obtain an appropriate radiographic density. The Gammex RMI model RMI 841S (Gammex RMI; Middleton, WI) dose area product meter has an aluminum equivalent of less than 0.5 mm. The Nuclear Associates model Diamentor M2 (Nuclear Associates, Division of Victoreen, Inc.; Carle Place, NY) dose area product meter an aluminum equivalent of 0.5 mm. The aluminum equivalent of the prototype ionization chamber is not larger than that of the dose area product meters and therefore the aluminum equivalent of the prototype ionization chamber is not excessive for its stated purpose.

Energy Rate Dependence and Bias Voltage Selection

The energy rate dependence of the prototype device was evaluated with the use of test equipment which included a Siemens radiographic and fluoroscopic unit, a Radcal dosimeter, a Fluke multimeter, an Ortec power supply and a high voltage cable.

The focal spot location of the radiographic x-ray tube was determined through the use of the following protocol. The x-ray table and the x-ray tube were leveled using a bubble level. A large line pair phantom was attached to the aperture of a test stand. The x-ray tube was aligned to the center of the phantom. A radiograph was taken of the phantom using a fine grain film. The generator technique factors of 50 kVp, 50 mA and 1.0 s and the small focal spot were utilized to produce a radiographic gross optical density of 1.1. The fine grain film, the low kVp and mA, the small focal spot and an optimal optical density produced a sharp image for precise edge delineation. The distances between the phantom and the film, the leaded edges of the phantom and the corresponding image edges on the radiograph were measured. An approximation of the focal spot location was determined using a similar triangles calculation with the measured distances. The focal spot location was marked on the x-ray tube housing.

The voltage output of the Ortec power supply was connected to the high voltage electrode of the prototype ionization chamber. A Fluke multimeter was installed in the circuit so that the voltages supplied to the high voltage electrode of the prototype ionization chamber were monitored. When the prototype ionization chamber was mounted to the bottom of the x-ray collimator the distance from the source to the middle of the prototype ionization chamber was 29.5 cm. The two turns-dial counters of the prototype control module were rotated to display 300.0 cm. The two scaling networks of the prototype control module were adjusted to have negligible attenuation on the computational unit output voltage.

The reference Radcal ionization chamber was positioned at a SDD of 111.4 cm. The relatively large SDD was employed so that the energy rate dependence of the reference dosimeter would be minimized. The x-ray field size was 20 cm x 20 cm at a source-to-image receptor distance (SID) of 100 cm. Five sets of generator technique factors were selected which progressively increased the x-ray tube output.

The first set of the generator technique factors was selected. Four exposures were made and the Radcal dosimeter was used to measure exposure and exposure time of each irradiation. The prototype ionization chamber was then

mounted to the bottom of the x-ray collimator. The voltage
output of the Ortec power supply was increased in specific
intervals as the prototype device voltage measurements were
documented upon irradiation. The prototype ionization
chamber was removed from the collimator and four additional
exposures were measured by the Radcal dosimeter to check for
constancy. This procedure was repeated for the other four
sets of generator technique factors.

Figure 5-3 is a plot of the bias potential of the
prototype ionization chamber versus the relative collection
efficiency for five mid-chamber exposure rates. The
relative collection efficiency at a specific bias potential
and exposure rate was defined as the observed voltage
measurement divided by the voltage measurement at a bias
potential of 1000 volts. The exposure rates at the middle
of the prototype ionization chamber were calculated by
applying an inverse-square distance correction to the Radcal
measurements. A bias potential of 500 volts was selected
for the prototype ionization chamber. As shown in Figure
5-4, the prototype ionization chamber relative collection
efficiency at an exposure rate of 97 R/s and a bias
potential of 500 volts was greater than 0.98. The 97 R/s
exposure rate at the middle of the prototype ionization
chamber was the approximate maximum exposure rate allowable
from the Siemens radiographic equipment utilized.
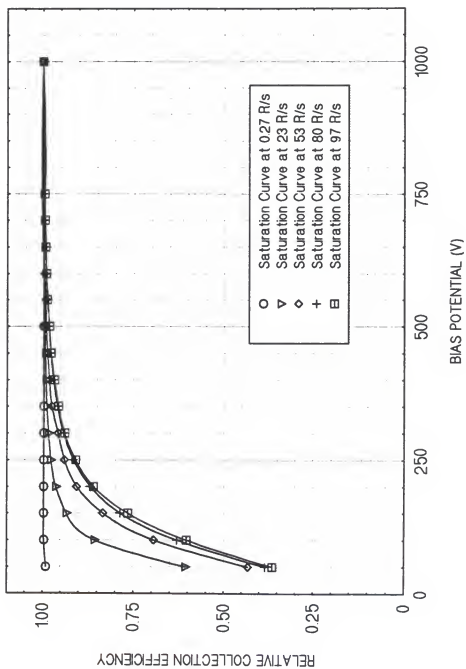
Figure 5-3: Saturation curves at different exposure rates
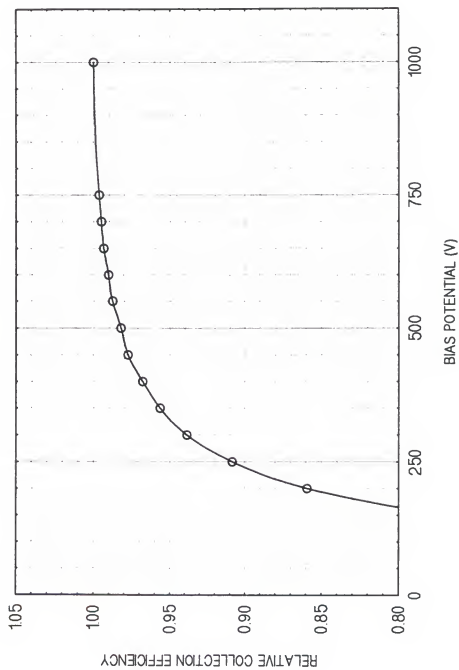
Figure 5-4: Saturation curve at 97 R/s

Radcal specifies an energy rate dependence of ± 5% over the exposure rate range from 0.4 mR/s to 80 R/s for the ionization chamber utilized. The energy rate dependence for the prototype device with a bias potential of 500 volts was approximately 1% over the same range of exposure rates. The relatively small energy rate dependence of the prototype device with a bias potential of 500 volts is clearly acceptable for its stated purpose.

Capacitor Selection and Calibration

The calibration of the prototype device was evaluated with the use of test equipment which included a Siemens radiographic and fluoroscopic unit, a Radcal dosimeter, a Machlett Dynalyzer, a Nuclear Associates thermometer and a National Weather Service barometer. The radiographic generator technique factors were selected to produce a Dynalyzer measurement of approximately 80 kVp. The relatively low exposure rate selected minimized the Radcal dosimeter energy rate dependence effect. The prototype ionization chamber was mounted to the bottom of the x-ray collimator at a SDD of 29.5 cm. The turns-dial counters were rotated so that the SDD counter displayed 29.5 cm and the SSD counter displayed 70.0 cm. The two scaling networks of the prototype control module were adjusted to have negligible attenuation on the computational unit output

voltage. The capacitance of the prototype feedback capacitor was 5×10^{-9} farad. The Radcal ionization chamber was positioned at a SDD of 70.0 cm. The x-ray field size was 20 cm x 20 cm at a SID of 100 cm.

Several exposures were made while documenting the measurements from both the prototype device and the Radcal dosimeter. The average prototype measurement in millivolts was divided by the average Radcal measurement in milliroentgen to obtain a scaling factor. The scaling factor was multiplied by the capacitance of the prototype feedback capacitor to obtain a capacitance value of 3.6×10^{-9} farad. Changing the capacitance of the prototype feedback capacitor to 3.6×10^{-9} farad would roughly provide a one-to-one correspondence between the prototype measurement in mV to the Radcal measurement in mR. The selected capacitance of the first feedback capacitor is 3.6×10^{-9} farad.

Given a maximum electrometer output of approximately 12 volts, a feedback capacitance of 3.6×10^{-9} farad, a Radcal measurement of 274 mR at a SDD of 70.0 cm, the computational unit output voltage at a SDD of 29.5 cm and a SSD of 70.0 cm would be approximately 2100 mV which is slightly higher than the maximum measurement capability of the control unit digital voltage meter which is 1999 mV. Thus the prototype

device would be capable of measuring an exposure range from 1 mR to 1999 mR at a SDD of 29.5 cm and a SSD of 70.0 cm.

The capacitance of the second feedback capacitor of the prototype device was chosen to be 3.0×10^{-6} farad. This feedback capacitance would allow for an exposure measurement range from 1 R to 1800 R at a SDD of 29.5 cm and a SSD of 70.0 cm.

A precise calibration of the prototype device was conducted once the selected capacitors were installed. The experimental set-up was similar to that described above. A series of ten exposures were measured by the prototype device and the Radcal dosimeter. The measurements of the prototype device were corrected for temperature and pressure. The measurements of the Radcal dosimeter were corrected for energy dependence based on values obtained from its Accredited Dosimetry Calibration Laboratory (ADCL) calibration. The Radcal dosimeter automatically corrects for temperature and pressure.

Throughout the exposure series the control module scaling network was adjusted so that the corrected prototype measurement was identical to the corrected Radcal measurement. A second series of ten exposures were measured by the prototype device and the Radcal dosimeter. The second series of exposures was used to check for similarity and constancy of the measurements. Both feedback capacitors

and their associated scaling networks were calibrated using the described calibration procedure.

Linearity Dependence

The prototype device linearity upon multiple exposures was evaluated with the use of a Siemens radiographic and fluoroscopic unit. The prototype ionization chamber was mounted to the bottom of the x-ray collimator. The turns-dial counters were rotated so that the SDD counter displayed 29.5 cm and the SSD counter displayed 70.0 cm. The Radcal ionization chamber was positioned at a SDD of 70.0 cm. The field size was 20 cm x 20 cm at a SID of 100 cm. The generator technique factors were selected so that a cumulative series of eleven exposures would not exceed the prototype device full-scale display. Eleven similar exposures were made and the cumulative measurements of the prototype device and the Radcal dosimeter were documented.

Figure 5-5 is a plot of the cumulative Radcal dosimeter measurements versus those of the prototype device with the 3.6×10^{-9} farad capacitor and associated scaling network selected. The percent difference of the eleventh cumulative measurement between the reference dosimeter and the prototype device was zero at three significant figures. The linearity of exposure measurements between prototype device
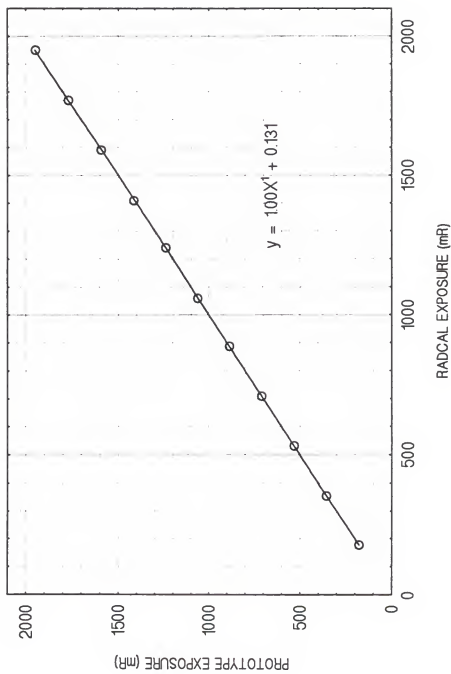
Figure 5-5: Multiple exposure linearity (3600 pF)

and the Radcal dosimeter was nearly ideal.   Figure 5-6 is a
plot of the cumulative Radcal dosimeter measurements versus
those of the prototype device with the 3.0 x 10^{-6} farad
capacitor and associated scaling network selected.   The
percent difference of the eleventh cumulative measurement
between the reference dosimeter and the prototype device was
0.20% at three significant figures.   The linearity of
exposure measurements between the prototype device and the
Radcal dosimeter was nearly ideal.

Energy Dependence

The energy dependence of the prototype ionization
chamber was evaluated with the use of test equipment which
included a Siemens radiographic and fluoroscopic unit, a
Machlett Dynalyzer, a Keithley kVp divider and readout, a
Radcal dosimeter, a test stand, a selection of different
thickness 1100 alloy aluminum filters, a lead plate with
aperture and a Nuclear Associates thermometer.

Overhead x-ray tube

Eighteen sets of generator technique factors were
selected for use on the overhead radiographic x-ray tube.
The kVps of technique factors sets gradually increased in
steps.   The kVp was measured for each set of technique
factors using a Machlett Dynalyzer and the measured kVps
ranged from 45 to 128.   The x-ray beam quality of each set
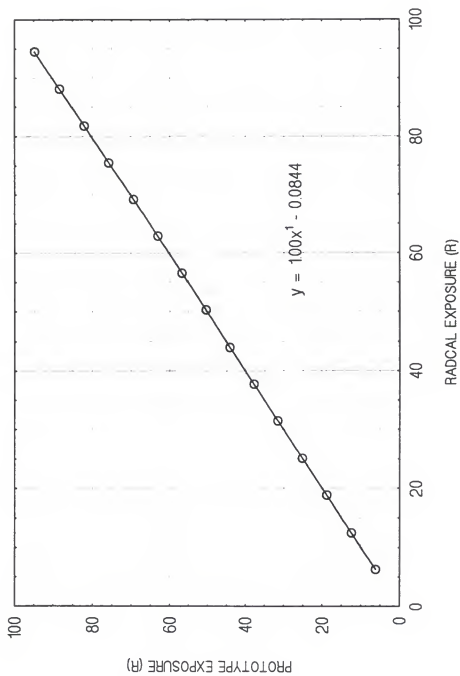
Figure 5-6: Multiple exposure linearity (3.0 μF)

of technique factors was characterized by a first half-value layer (HVL). The procedures used to determine the HVLs were described in the section titled Aluminum Equivalent. Figure 5-7 is a plot of the x-ray tube potential versus the x-ray beam quality for the overhead radiographic x-ray tube. A linear relationship between the measured kVp and HVL was observed.

The energy dependence of the prototype ionization chamber was evaluated using the following procedures. The prototype ionization chamber was attached to the bottom of the overhead radiographic x-ray tube collimator. The turns-dial counters were rotated so that the SDD counter displayed 29.5 cm and the SSD counter displayed 70.0 cm. The Radcal ionization chamber was positioned at a SDD of 70.0 cm. The x-ray field size was 20 cm x 20 cm at a SID of 100 cm. A series of four exposures were measured by the prototype device and the Radcal dosimeter at each of the eighteen sets of generator technique factors discussed above. The measurements of the prototype device were corrected for temperature and pressure. The measurements of the Radcal dosimeter were corrected for energy dependence based on values obtained from its ADCL calibration shown in Figure 5-8. The Radcal dosimeter automatically corrects for temperature and pressure.
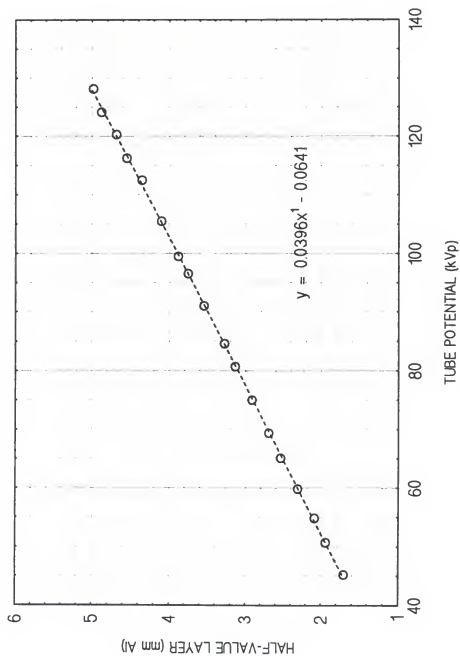
Figure 5-7: Linearity of tube potential and beam quality (overhead x-ray tube)
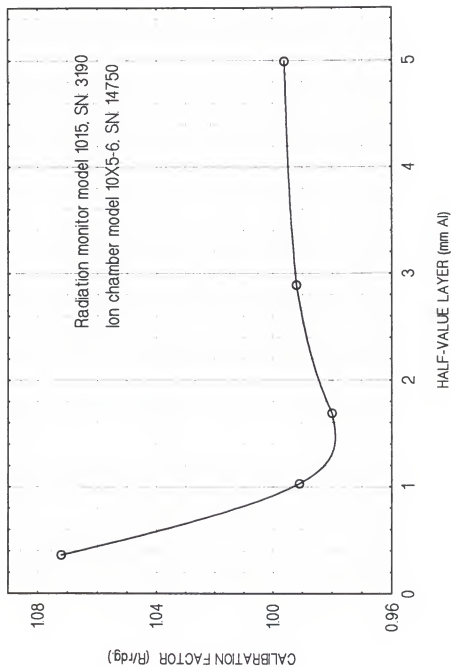
Figure 5-8: ADCL calibration for energy dependence of Radcal system

The average Radcal corrected measurement was divided by the average prototype corrected measurement at each set of generator technique factors. The resultant value was the calibration factor of the prototype ionization for that particular set of generator technique factors. The x-ray beam quality of each set of technique factors was characterized by its first HVL. Figure 5-9 is a plot of the x-ray beam quality versus the prototype ionization chamber calibration factor conducted on the overhead radiographic x-ray tube.

The x-ray tube potentials commonly employed in the clinic for radiographic diagnostic procedures other than mammography and small extremity examinations range from 60 to 120 kVp. Using Figure 5-7, the HVLs associated with 60 and 120 kVp are 2.31 and 4.68 mm of aluminum respectively. Using Figure 5-9, the minimum and maximum calibration factors between HVLs of 2.31 and 4.68 mm of aluminum are 0.980 and 1.071 respectively.

Undertable x-ray tube

Eight sets of generator technique factors were selected for use on the undertable fluoroscopic x-ray tube. The kVps of technique factors sets gradually increased in steps. The kVp was measured for each set of technique factors using a Keithley kVp divider and readout. The measured kVps ranged from 51 to 121. The x-ray beam quality of each set of
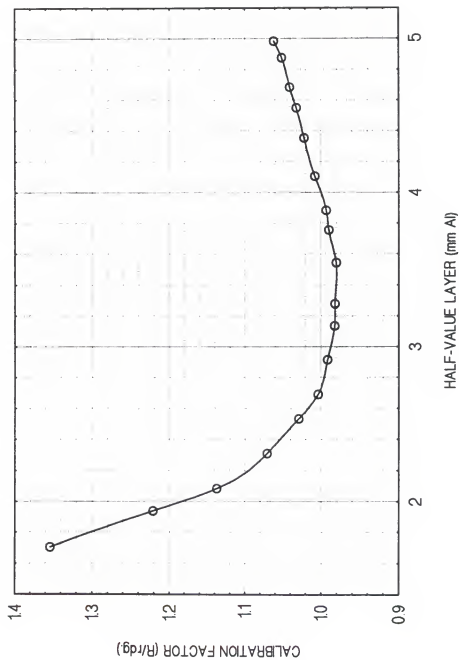
Figure 5-9: Energy dependence of prototype device (overhead x-ray tube)

technique factors was characterized by a first half-value layer (HVL).

The HVLs of the undertable fluoroscopic x-ray tube were determined through the use of the following procedures. The Radcal ionization chamber was attached to the test stand. A lead plate with a 10 cm x 10 cm aperture was placed in the filter slot of the stand and stand was placed up-side-down. The x-ray field was centered to the aperture using fluoroscopy. The x-ray tube collimator was adjusted so that the x-ray field size at the aperture of the lead plate was slightly smaller than the aperture. Using the spot film device, different filtration thicknesses were exposed and the results documented for the selected sets of technique factors. The HVLs were determined by plotting the added aluminum filtration thickness versus the relative exposure. Figure 5-10 is a plot of the x-ray tube potential versus the x-ray beam quality for the undertable fluoroscopic x-ray tube. A linear relationship between the measured kVp and HVL was observed.

The energy dependence of the prototype ionization chamber when mounted to an undertable x-ray tube was evaluated using the following procedures. The prototype ionization chamber was attached to bottom of the undertable fluoroscopic x-ray tube collimator. The turns-dial counters were rotated so that the SDD counter displayed 29.5 cm and
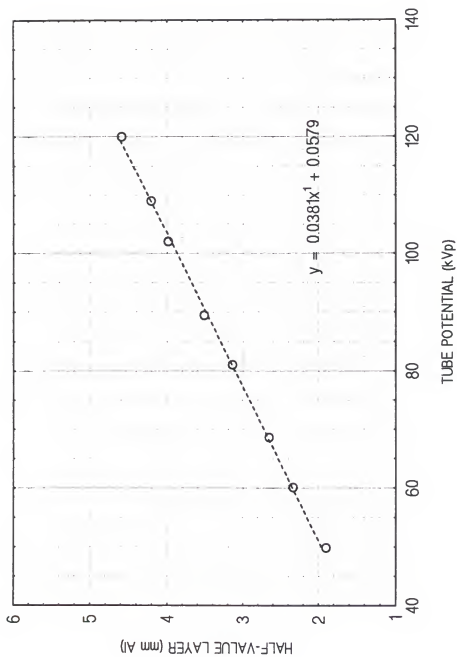
Figure 5-10: Linearity of tube potential and beam quality (undertable x-ray tube)

the SSD counter displayed 69.7 cm. The Radcal ionization chamber was positioned at a SDD of approximately 69.7 cm which was located 8.4 cm above the x-ray table. The x-ray field size was approximately 20 cm x 20 cm at a SID of 100 cm. A series of four exposures were measured by the prototype device and the Radcal dosimeter at each of the eight sets of generator technique factors discussed above. The measurements of the prototype device were corrected for temperature and pressure. The measurements of the Radcal dosimeter were corrected for energy dependence based on values obtained from its ADCL calibration shown in Figure 5-8. The Radcal dosimeter automatically corrects for temperature and pressure.

The average Radcal corrected measurement was divided by the average prototype corrected measurement at each set of generator technique factors. The resultant value was the calibration factor of the prototype ionization for that particular set of generator technique factors. The x-ray beam quality of each set of technique factors was characterized by its first HVL. Figure 5-11 is a plot of the x-ray beam quality versus the prototype ionization chamber calibration factor conducted on the overhead radiographic x-ray tube.

The x-ray tube potentials commonly employed in the clinic for fluoroscopic diagnostic procedures range from 60
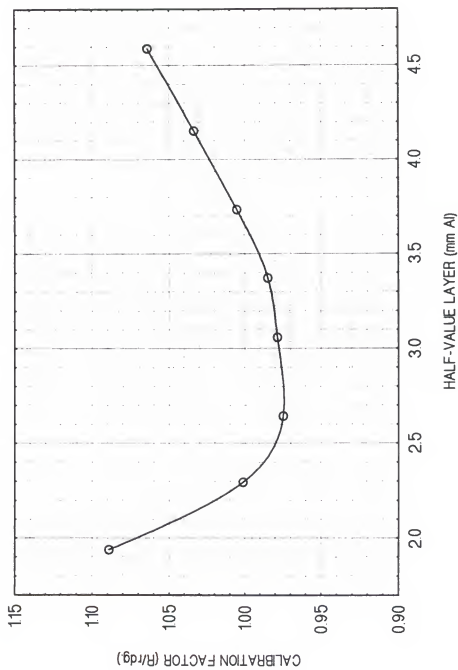
Figure 5-11: Energy dependence of prototype device
(undertable x-ray tube)

to 120 kVp. Using Figure 5-10, the HVLs associated with 60
and 120 kVp are 2.28 and 4.59 mm of aluminum respectively.
Using Figure 5-11, the minimum and maximum calibration
factors between HVLs of 2.28 and 4.59 mm of aluminum are
0.974 and 1.064 respectively.

Undertable x-ray tube with added table filtration

Eight sets of generator technique factors were selected
for use on the undertable fluoroscopic x-ray tube with an
added filtration of 0.99 mm of aluminum to the x-ray table.
The aluminum equivalent of the combination consisting of the
x-ray table and the added filtration was 2.0 mm of aluminum
which is the maximum aluminum equivalent for a patient
support in a imaging system that the Federal regulations
allow (Federal Register 1993b). The kVps and the HVLs were
measured in a similar manner to that described in the
section above. Figure 5-12 is a plot of the x-ray tube
potential versus the x-ray beam quality for the undertable
fluoroscopic x-ray tube with additional filtration added. A
linear relationship between the measured kVp and HVL was
observed.

The energy dependence of the prototype ionization
chamber when mounted to an undertable x-ray tube with added
table filtration was evaluated using similar procedures to
that in the section above. Figure 5-13 is a plot of the x-
ray beam quality versus the prototype ionization chamber
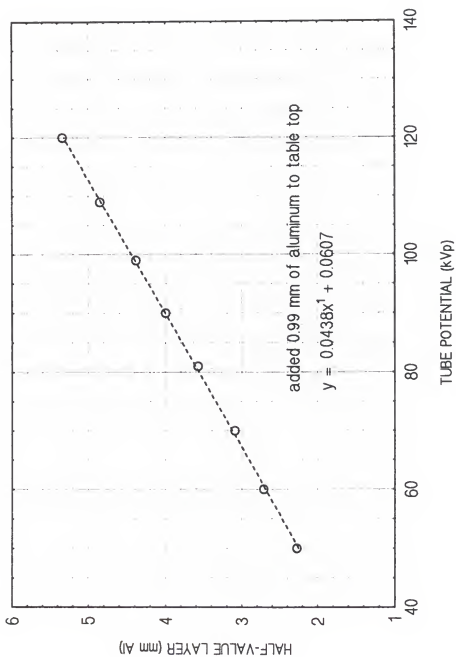
Figure 5-12: Linearity of tube potential and beam quality (undertable x-ray tube with added filtration)
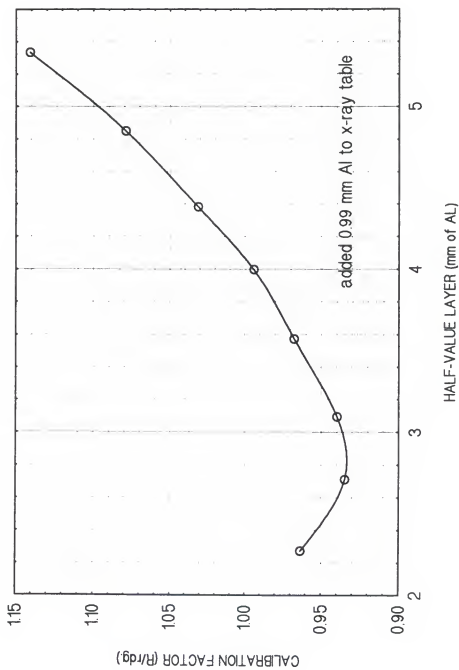
Figure 5-13: Energy dependence of prototype device
(undertable x-ray tube with added filtration)

calibration factor conducted on the overhead radiographic x-ray tube.

The x-ray tube potentials commonly employed in the clinic for fluoroscopic diagnostic procedures range from 60 to 120 kVp. Using Figure 5-12, the HVLs associated with 60 and 120 kVp are 2.68 and 5.28 mm of aluminum respectively. Using Figure 5-13, the minimum and maximum calibration factors between HVLs of 2.68 and 5.28 mm of aluminum are 0.933 and 1.134 respectively.

Figure 5-14 is a plot of the three calibration curves for the prototype ionization chamber as presently calibrated. If the overhead x-ray tube calibration was optimized, its energy dependence would be ± 4.6% over the kVp range from 60 to 120 kVp. If the undertable x-ray tube calibration was optimized, its energy dependence would be ± 4.5% over the kVp range from 60 to 120 kVp. If the undertable x-ray tube calibration with the 2 mm aluminum equivalent table was optimized, its energy dependence would be ± 10% over the kVp range from 60 to 120 kVp.

Nuclear Associates specifies that its dose area product meter has a energy dependence of ± 5% between 50 and 150 kVp or between 1.5 mm and 6 mm of aluminum HVL. The Nuclear Associates device is commonly calibrated on an overhead x-ray tube. The prototype ionization chamber has a larger energy dependence than that of the dose area product meter.
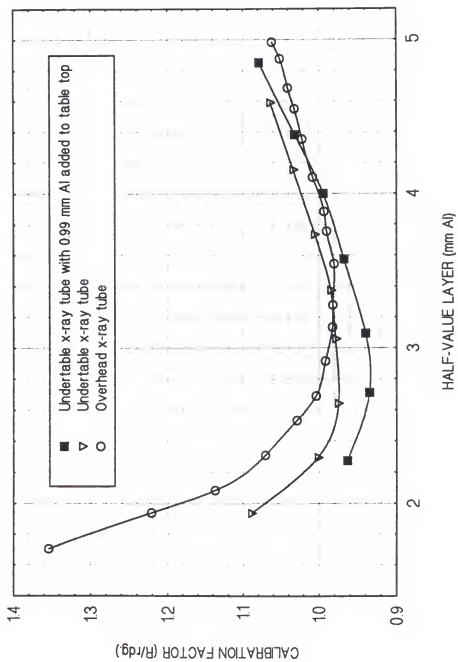
Figure 5-14: Energy dependence of prototype device under different testing protocols

The prototype ionization chamber energy dependence over the clinically used kVp range is within ± 5.2% for either radiography or fluoroscopy. Under the unusual circumstance that the aluminum equivalent of the fluoroscopic x-ray table is 2.0 mm, the prototype ionization chamber energy dependence increases to ± 10%. Although the prototype ionization chamber energy dependence is larger than desired, the prototype device energy response is acceptable for its stated purpose.

X-Ray Field Size Dependence

The field size dependence of the prototype ionization chamber was evaluated with the use of test equipment which included a Siemens radiographic and fluoroscopic unit, a Machlett Dynalyzer, a Radcal dosimeter and a Nuclear Associates thermometer. The prototype ionization chamber was mounted to the bottom of the overhead x-ray collimator. The turns-dial counters were rotated so that the SDD counter displayed 29.5 cm and the SSD counter displayed 70.0 cm. The Radcal ionization chamber was positioned at a SDD of 70.0 cm. The nearest backscatter object was the room floor which was located 160 cm from the Radcal ionization chamber. A set of generator technique factors was selected. The measured x-ray tube potential of the selected technique

factors was 85 kVp and the Machlett Dynalyzer was used to perform that measurement.

The x-ray field size was varied through a range from 10 cm x 10 cm to 45 cm x 45 cm at a SID of 100 cm. A series of four exposures using the same technique factors were made at each selected x-ray field size. The measurements of the prototype device were corrected for temperature and pressure. The measurements of the Radcal dosimeter were corrected for energy dependence based on values obtained from its ADCL calibration. The Radcal dosimeter automatically corrects for temperature and pressure. The average prototype corrected measurement was divided by the average Radcal corrected measurement at each x-ray field size. The data were then normalized to the value at the 20 cm x 20 cm x-ray field size which was the field size used during calibration.

Figure 5-15 is a plot of the x-ray field size at a SID of 100 cm versus the prototype normalized relative response upon irradiation. If the x-ray field size is less than 20 cm x 20 cm or 400 cm^2, the prototype ionization has a smaller response relative to the reference ionization chamber upon irradiation. If the x-ray field size is greater than 20 cm x 20 cm, the prototype ionization has a larger response relative to the reference ionization chamber upon irradiation.
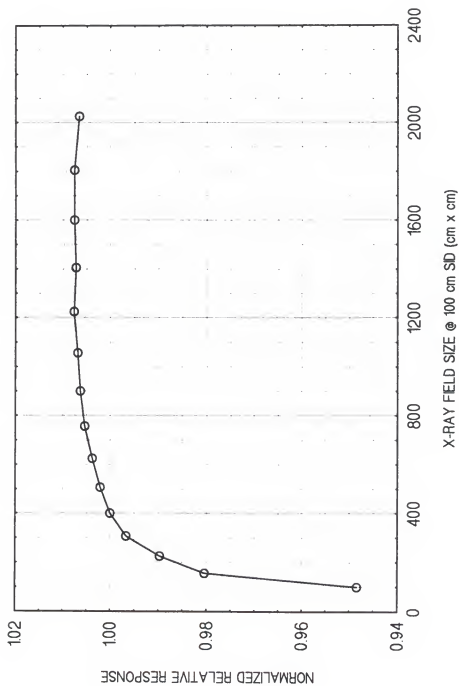
Figure 5-15: Field size dependence

The sensitive volume of the prototype ionization chamber must be irradiated over its entire volume in order for a proportionality to exist between its collected charges and the collected charges of another ionization chamber that had its sensitive volume fully irradiated. The diameter of the cylindrical shaped sensitive volume of the prototype ionization chamber is approximately 17.6 mm. Given a SDD of 29.5 cm, a 17.6 cm x 17.6 cm x-ray field size present at the middle of the prototype ionization chamber presents a 20.2 cm x 20.2 cm field size at a SID of 100 cm. Thus the prototype ionization chamber should show an under-response relative to the Radcal ionization chamber upon irradiation when the x-ray field size is approximately 20 cm x 20 cm or less. At x-ray field sizes larger than 20 cm x 20 cm, the prototype ionization chamber should respond in a manner that is similar to the Radcal ionization chamber upon irradiation.

The 20 cm x 20 cm x-ray field size that was selected for the prototype ionization chamber calibration was inappropriate. Based on the shape of the curve in Figure 5-15, a field size of 30 cm x 30 cm that is on the plateau of the curve would have been more appropriate. The x-ray field sizes commonly employed in the clinic for radiographic and fluoroscopic procedures other than mammography and small extremity examinations range from approximately 15 cm x 15

cm to 35 cm x 43 cm. For the clinically used range of x-ray field sizes, the response of the prototype ionization chamber relative to the Radcal ionization chamber varies by approximately ± 0.9%.

The ± 0.9% difference in the relative response over the clinically used range of x-ray field sizes could be reduced by reducing the diameter of the cylindrically shaped sensitive volume of the prototype ionization chamber. In other words, the diameter of the prototype ionization chamber collection electrode could be reduced to minimize the x-ray field size dependence. The x-ray field size dependence of the prototype device is relatively small over the clinically used range of field sizes and therefore the prototype device is acceptable for its stated purpose.

Stem Dependence

Stem dependence refers to the relative signal contribution arising from the electrical conductor or stem leading to the sensitive volume of the ionization chamber as compared with the signal or charges collected in the sensitive volume upon irradiation. In a properly designed ionization chamber the signal arising from the stem should be negligible compared to the signal arising from the sensitive volume.

The stem dependence of the prototype ionization chamber was evaluated. The prototype ionization chamber was mounted to the bottom of a x-ray collimator on a Siemens radiographic unit. The turns-dial counters were rotated so that the SDD counter was 30.1 cm and the SSD counter was 70.0 cm. The Radcal dosimeter was positioned at an SDD of 70 cm, on the central ray of the x-ray tube and so that its stem was perpendicular to the stem of the prototype ionization chamber.

A series of four exposures were made with the collimator adjusted to a field size of 10 cm x 45 cm at a SSD of 100 cm. The exposure measurements of both devices were documented. Another series of four exposures were made with the collimator adjusted to a field size of 45 cm x 10 cm at a SSD of 100 cm. The exposure measurements of both devices were documented. The average prototype exposure measurement was divided the average Radcal measurement for each field size orientation. The percent difference between the two ratios was 0.03%. Thus the magnitude of the prototype stem dependence was very similar to that of the reference dosimeter. The stem dependence magnitude of the prototype ionization chamber is acceptable for its stated purpose.

Patient Backscatter Dependence

The prototype ionization chamber dependence on patient backscatter was evaluated with the use of test equipment which included a Siemens radiographic and fluoroscopic unit, a Machlett Dynalyzer and a water phantom. The ICRU states that a standard phantom for radiography and fluoroscopy of the abdomen is a cuboid water filled phantom with the dimensions of 30 cm x 30 cm x 30 cm and a container made from acrylic (ICRU 1992). The water phantom utilized consisted of a 30 cm x 30 cm x 36 cm nagalene container that was filled with 30 cm of water. An suitable acrylic container was not available.

The prototype ionization chamber was mounted to the bottom of the overhead x-ray collimator. The turns-dial counters were rotated so that the SDD counter displayed 29.5 cm and the SSD counter displayed either 40.0 or 70.0 cm. The water phantom was placed on top of the x-ray table and centered to the x-ray field. The distance from the x-ray tube focus to the top surface of the water phantom was either 40.0 or 70.0 cm. The x-ray field size was 30.0 cm x 30.0 cm at a SID of 100 cm.

Eight sets of generator technique factors were selected for use on the overhead radiographic x-ray tube. The kVps of technique factors sets gradually increased in steps. The kVp was measured for each set of technique factors using a

Machlett Dynalyzer and the measured kVps ranged from 51 to
120. The HVLs of each set of technique factors were
determined in the energy dependence section. A plot of the
HVLs versus the x-ray tube potential is shown in Figure 5-7.
At each set of technique factors, four exposures were made
with water phantom in the x-ray field and four exposures
were made without the water phantom in the x-ray field and
all exposures were measured by the prototype device. This
procedure was conducted at source-to-water surface distance
of 40.0 cm and the procedure was conducted a second time at
source-to-water distance of 70.0 cm.

Figure 5-16 is a plot of the percent differences
between the prototype measurements with and without the
water phantom in the x-ray field at two source-to-phantom
distances. When the source-to-phantom distance was 40.0 cm,
the backscatter contribution to the prototype measurement
over the clinically used kVp range from 60 to 120 kVp varied
from 2.1 to 3.7%. When the source-to-phantom distance was
70.0 cm, the backscatter contribution to the prototype
measurement over the clinically used kVp range varied from
0.19 to 0.40%. Therefore the prototype ionization chamber
has a relatively small dependence on patient backscatter
upon irradiation and this small dependence is acceptable for
its stated purpose.

The prototype device's measurement uncertainty can be estimated by evaluating the square root of the sum of the square of the specific uncertainties. For the worst case clinical scenario of SDDs, SSDs, kVps, x-ray field sizes and exposure rates, an estimate of the prototype device's measurement uncertainty is approximately ± 6.3%.
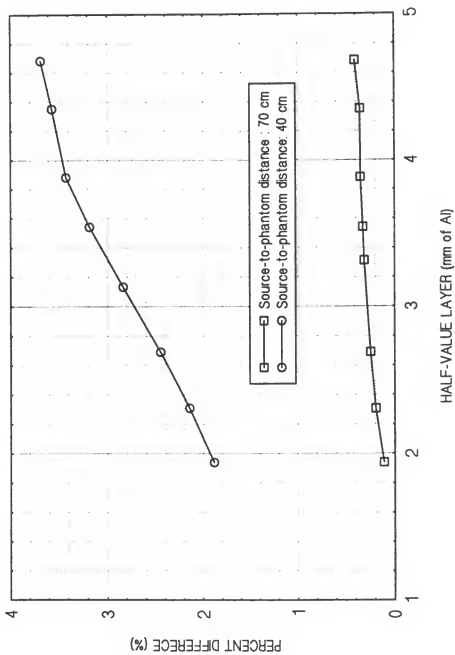
Figure 5-16: Dependence on patient backscatter

CHAPTER 6
SUMMARY AND CONCLUSIONS

In order to obtain the information necessary for an actual dose assessment of a patient, the medical physicist generally requires an assessment of the entrance skin exposure free-in-air (ESE). Once the measurement of ESE has been obtained, the physicist can then apply this information to published tables which contain relative factors to obtain fetal dose estimates, organ dose estimates and equivalent dose estimates.

At the present time a device does not exist which measures ESE directly at the time of the patient x-ray procedure. A prototype device has been designed and built for the purpose of measuring ESE directly at the time of the patient x-ray procedure. The design of the prototype device is based on a practical ionization chamber.

The prototype device is contained in three modules. The first module consists of a parallel-plate ionization chamber, an electrometer and the mounting brackets for collimator port attachment. The second module or control module houses the computational unit circuitry, the scaling circuitry, the switching and reset circuitry and the digital

voltage meter. The third module or the power supply module houses the power supplies.

The materials selected to construct the parallel-plate ionization chamber were chosen to maximize the visible light transmittance while maintaining the characteristics necessary for a practical ionization chamber. The visible light transmittance was approximately 49%. The acrylic substrate thickness of the parallel-plate ionization chamber is 2.4×10^{-1} mm which ensured charged particle equilibrium and mechanical stability.

The wall of the parallel-plate ionization chamber is constructed of an acrylic substrate, a silicon hardcoat and an outer coating of indium tin oxide. The manufacturer stated that the thickness of the silicon hardcoat is approximately 0.9 μm and thickness of the indium tin oxide coating (ITO) is approximately 2000 Angstroms. The varying resistances of the plates received from the manufacturer indicate that the ITO coating thicknesses vary and the approximate 2000 Angstrom thickness specified by the manufacturer is incorrect.

The air-equivalency of the parallel-plate ionization chamber wall based upon the thicknesses stated above was estimated by two approaches. The interaction data method yielded results which indicated that the prototype ionization chamber has slightly larger Compton mass

attenuation coefficients relative to air, smaller photoelectric mass attenuation coefficients relative to air at photon energies less than 40 keV and larger photoelectric mass attenuation coefficients relative to air at energies above 40 keV. The calculated effective atomic number of air was 7.78 and that of the prototype ionization chamber wall was 7.66.

The etching process and the handling of the parallel-plates enhanced the artifacts present before the etching process and created additional artifacts. In the future, the etching processes or the masking processes during the ITO deposition should be controlled by the manufacturer in order to produce a product with fewer artifacts.

The leakage current at the electrometer input was approximately 9×10^{-15} ampere and this could be reduced by filling the electrometer housing with ceresin wax. The percent error of the inverse square computational network was approximately $\pm 1\%$ for the range of clinically used SDDs and SSDs.

The aluminum equivalent of the prototype ionization chamber was approximately 0.46 mm of aluminum. The energy rate dependence of the prototype device with a bias potential of 500 volts was less than 2% at an exposure rate of 97 R/s. The prototype device is capable of measuring an exposure range from 1 mR to 1999 mR and from 1 R to 1800 R

at a SDD of 29.5 cm and a SSD of 70.0 cm. The linearity of exposure measurements between the prototype device and the reference dosimeter was nearly ideal.

The energy dependence of the prototype ionization chamber when the ionization chamber was mounted to an overhead x-ray tube was ± 4.6% over a range of beam qualities from 2.3 to 4.7 mm of aluminum. The energy dependence of the prototype ionization chamber when the ionization chamber was mounted to an undertable x-ray tube was ± 4.5% over a range of beam qualities from 2.3 to 4.7 mm of aluminum. The energy dependence of the prototype ionization chamber when the ionization chamber was mounted to an undertable x-ray tube and filtration was added to the table was ± 10% over a range of beam qualities from 2.7 to 5.3 mm of aluminum.

The energy dependence of the prototype ionization chamber showed an under-response at both lower and higher beam qualities. The under-response at lower beam qualities was due to the attenuation effect from the utilization of an acrylic substrate thickness larger than that required for charge particle equilibrium. The under-response at higher beam qualities was not predicted by the air-equivalent calculations. If the ITO coating thickness was actually less than 2000 Angstroms as suggested by the observed

varying resistances, then the under-response at higher beam qualities is predictable.

The x-ray field size dependence of the prototype ionization chamber varied by ± 0.9% relative to the reference dosimeter over the range of field sizes from 15 cm x 15 cm to 35 cm x 43 cm. The x-ray field size dependence of the prototype ionization chamber could be reduced by decreasing the diameter of the collection electrode. The stem dependence of the prototype ionization chamber was approximately 0.03%.

The patient backscatter dependence when the source-to-phantom distance was 70 cm varied from 0.19 to 0.40% over the range of beam qualities from 1.9 to 4.7 mm of aluminum. The patient backscatter dependence when the source-to-phantom distance was 40 cm varied from 2.1 to 3.7% over the range of beam qualities from 1.9 to 4.7 mm of aluminum.

For the worst case clinical scenario of SDDs, SSDs, kVps, x-ray field sizes and exposure rates, an estimate of the overall measurement uncertainty was approximately ± 6.3%. Therefore, the results of the quantitative evaluations demonstrate that the prototype device is suitable for its stated purpose of measuring ESE directly at the time of the patient x-ray procedure.

APPENDIX A
SAMPLE CALCULATION OF PHOTON INTERACTION
COEFFICIENTS OF AIR AT 40 keV

Photoelectric Mass Attenuation
Coefficients at 40 keV

Element	Atomic Weight (g/mole)	Elemental Fraction by Weight	Cross Section (barn/atom)	μ_{photo}/ρ (cm^2/g)
H	1.00797	3.1346E-7	--	--
He	4.0026	6.9152E-7	0.00158	1.6440E-10
C	12.01115	1.3779E-4	0.423	2.9225E-6
N	14.0067	7.5500E-1	0.883	2.8665E-2
O	15.9994	2.3200E-1	1.65	1.4409E-2
Ne	20.183	1.2553E-5	4.65	1.7418E-6
Ar	39.948	1.2837E-2	64.6	1.2502E-2
Kr	83.80	2.8956E-6	1110	2.3099E-5
Xe	131.30	3.6295E-7	4810	8.0077E-6

Column 1: Elemental constituents of air (Sax and Lewis 1987)

Column 2: Elemental atomic weight (USDHEW 1970)

Column 3: Derived from constituent percent by volume of air
(Sax and Lewis 1987)

Column 4: Interaction coefficients (Storm and Israel 1970)

Column 5: cm^2/g = (barns/atom)(10^{-24} cm^2/barn)(6.02252 x

10^{23} atoms/mole)(elemental fractional

weight)/(g/mole)

Compton Mass Attenuation
Coefficients at 40 keV

Element	Atomic Weight (g/mole)	Elemental Fraction by Weight	Cross Section (barn/atom)	μ_{incoh}/ρ (cm^2/g)
H	1.00797	3.1346E-7	0.576	1.0788E-7
He	4.0026	6.9152E-7	1.14	1.1862E-7
C	12.01115	1.3779E-4	3.30	2.2799E-5
N	14.0067	7.5500E-1	3.81	1.2368E-1
O	15.9994	2.3200E-1	4.31	3.7639E-2
Ne	20.183	1.2553E-5	5.29	1.9815E-6
Ar	39.948	1.2837E-2	8.97	1.7360E-3
Kr	83.80	2.8956E-6	16.3	3.3920E-7
Xe	131.30	3.6295E-7	22.8	3.7957E-8

SAMPLE CALCULATION OF PHOTON INTERACTION COEFFICIENTS
OF PROTOTYPE IONIZATION CHAMBER WALL AT 40 keV

Physical Characteristics

Acrylic:

    a) chemical formula: $C_5H_8O_2$

    b) specific gravity: 1.180 g/cm^3

    c) plate thickness: 0.149 cm

    d) mass per unit area: 0.17582 g/cm^2/plate

    e) molecular weight: 100.11831 g/mole

Silicone hardcoat:

    a) chemical formula: $C_2H_5Si_3O_5$

    b) specific gravity: 1.45 g/cm^3

    c) coating thickness: $2(9 \times 10^{-5}$ cm)

    d) mass per unit area: 2.61×10^{-4} g/cm^2/plate

    e) molecular weight: 193.31715 g/mole

Indium tin oxide:

    a) chemical formula: 91% In_2O_3 + 9% SnO_2

    b) specific gravity: 6.65 g/cm^3

    c) coating thickness: $2(2.0 \times 10^{-5}$ cm)

    d) mass per unit area: 2.66×10^{-4} g/cm^2/plate

  e) molecular weight: In_2O_3: 277.6382 g/mole

                          SnO_2: 150.6888 g/mole

<u>Calculation of percent by weight of mixture</u>

Lucite:

  $(100\%)(0.17582)/(0.17582 + 2.61E-4 + 2.66E-4)$

  $= 99.70116\%$

Silicone hardcoat:

  $(100\%)(2.61E-4)/(0.17582 + 2.61E-4 + 2.66E-4)$

  $= 0.1480037\%$

Indium tin oxide:

  $(100\%)(2.66E-4)/(0.17582 + 2.61E-4 + 2.66E-4)$

  $= 0.1508390\%$

<u>Calculation of elemental fractional content by weight (W)</u>

$W(H) = 8(1.00797)(0.9970116)/(100.11831) +$

        $5(1.00797)(1.480037E-3)/(193.31715)$

        $= 8.03402E-2$

$W(C) = 5(12.01115)(0.9970116)/(100.11831) +$

        $2(12.01115)(1.480037E-3)/(193.31715)$

        $= 5.982391E-1$

$W(O)$ = 2(15.9994)(0.9970116)/(100.11831) +

5(15.9994)(1.480037E-3)/(193.31715) +

3(15.9994)(0.91)(1.50839E-3)/(277.6382) +

2(15.9994)(0.09)(1.50839E-3)/(150.6888)

= 3.195333E-1

$W(Si)$ = 3(28.086)(1.480037E-3)/(193.31715)

= 6.450796E-4

$W(In)$ = 2(114.82)(0.91)(1.50839E-3)/(277.6382)

= 1.135333E-3

$W(Sn)$ = (118.69)(0.09)(1.50839E-3)/(150.6888)

= 1.069275E-4

Photoelectric Mass Attenuation
Coefficients at 40 keV

Element	Atomic Weight (g/mole)	Elemental Fraction by Weight	Cross Section (barn/atom)	μ_{photo}/ρ (cm^2/g)
H	1.00797	8.0340E-2	--	--
●	12.01115	5.9824E-1	0.423	1.2688E-2
O	15.9994	3.1953E-1	1.65	1.9846E-2
Si	28.086	6.4508E-4	21.4	2.9602E-4
In	114.82	1.1353E-3	3450	2.0545E-2
Sn	118.69	1.0693E-4	3700	2.0075E-3

Column 1: Elemental constituents of prototype ionization
          chamber

Column 2: Atomic weight (USDHEW 1970)

Column 3: Elemental fraction by weight (W); calculated above

Column 4: Interaction coefficients (Storm and Israel 1970)

Column 5: cm^2/g = (barns/atom)(10^{-24} cm^2/barn)(6.02252 x

10^{23} atoms/mole)(elemental fractional

weight)/(g/mole)

Compton Mass Attenuation Coefficients at 40 keV

Element	Atomic Weight (g/mole)	Elemental Fraction by Weight	Cross Section (barn/atom)	μ_{incoh}/ρ (cm^2/g)
H	1.00797	8.0340E-2	0.00288	2.7649E-2
C	12.01115	5.9824E-1	0.409	9.8988E-2
O	15.9994	3.1953E-1	0.857	5.1840E-2
Si	28.086	6.4508E-4	3.68	9.9041E-5
In	114.82	1.1353E-3	84.5	1.2506E-4
Sn	118.69	1.0693E-4	88.7	1.1557E-5

APPENDIX C
CALCULATION OF EFFECTIVE ATOMIC NUMBER OF AIR

Element	Atomic Number	Atomic Weight	Elemental fraction by weight
H	1	1.00797	3.1346E-7
He	2	4.0026	6.9152E-7
C	6	12.01115	1.3779E-4
N	7	14.0067	7.5500E-1
O	8	15.9994	2.3200E-1
Ne	10	20.183	1.2553E-5
Ar	18	39.948	1.2837E-2
Kr	36	83.80	2.8956E-6
Xe	54	131.30	3.6295E-7

Column 1: Elemental constituents of air (Sax and Lewis 1987)

Column 2: Atomic number

Column 3: Atomic weight (USDHEW 1970)

Column 4: Elemental fractional content by weight

Given that m = 4.52896 from Figure 4-4.

Element	N_oZW/A	a	$aZ^{(m-1)}$
H	1.872892E17	6.229784E-7	6.229784E-7
He	2.080993E17	6.921989E-7	7.990124E-6
●	4.145363E19	1.378868E-4	7.684000E-2
●	2.272413E23	7.558707E-1	7.257126E2
O	6.986385E22	2.323875E-1	3.574219E2
Ne	3.745760E18	1.245948E-5	4.211724E-2
Ar	3.483527E21	1.158722E-2	3.117351E2
Kr	7.491612E17	2.491928E-6	7.738642E-1
Xe	8.989883E16	2.990297E-7	3.883851E-1

Column totals: 3.006351E23   9.999998E-1   1.396151E3

$Z_{eff} = (1.396151 \times 10^3)^{(1/3.52896)} = 7.78$

Column 1: Elemental constituents of air (Sax and Lewis 1987)

Column 2: Elemental number of electrons per gram

Column 3: Fractional number of electrons per element

APPENDIX D
CALCULATION OF EFFECTIVE ATOMIC NUMBER
OF PROTOTYPE IONIZATION CHAMBER WALL

Element	Atomic Number	Atomic Weight	Elemental fraction by weight
H	1	1.00797	8.034020E-2
C	6	12.01115	5.982391E-1
O	8	15.9994	3.195333E-1
Si	14	28.086	6.450796E-4
In	49	114.82	1.135333E-3
Sn	50	118.69	1.069275E-4

Column 1: Elemental constituents of prototype ionization
          chamber

Column 2: Atomic number

Column 3: Atomic weight (USDHEW 1970)

Column 4: Elemental fractional content by weight

Given that m = 4.24285 from Figure 4-4.

Element	N_oZW/A	a	$aZ^{(m-1)}$
H	4.800247E22	1.478288E-1	1.478288E-1
●	1.799781E23	5.542622E-1	1.849878E2
O	9.622339E22	2.963304E-1	2.513979E2
Si	1.936554E20	5.963829E-4	3.106322E0
In	2.917965E20	8.986191E-4	2.720370E2
SN	2.712839E19	8.354474E-5	2.700374E1

Column Totals: 3.247165E23   9.999999E-1   7.386806E2

$Z_{eff} = (7.386806 \times 10^2)^{(1/3.25285)} = 7.67$

Column 1: Elemental constituents of prototype ionization
          chamber

Column 2: Elemental number of electrons per gram

Column 3: Fractional number of electrons per element

REFERENCES

American Association of Physicists in Medicine.
    Standardized methods for measuring diagnostic x-ray
    exposures. Woodbury, NY; American Institute of Physics;
    AAPM Report 31; 1990.

American College of Radiology: Committee on Quality
    Assurance in Mammography. Medical physicist's manual
    (1992). Reston, VA: ACR; 1992.

Berger, M.J.; Seltzer, S.M. Stopping powers and ranges of
    electrons and positrons (2nd edition). U.S. Department
    of Commerce; National Bureau of Standards; NBSIR 82-
    2550-A; 1983.

Boutillon, M.; Perroche-Roux, A.M. Re-evaluation of the W
    value for electrons in dry air. Phys. Med. Biol.
    32:213-219; 1987.

Brent, R.L. The effects of embryonic and fetal exposure to
    x-ray, microwaves, and ultrasound. Clin. Obstet.
    26:484-510; 1983.

Burkhart, R.L.; Gross, R.E.; Jans, R.G.; McCrohan, J.L.Jr.;
    Rosenstein, M.; Rueter, F.G. Recommendations for
    evaluation of radiation exposure from diagnostic
    radiology examinations. Rockville, MD: U.S. Department
    of Health and Human Services; HHS Publication (FDA) 85-
    8247; 1985.

Burlington, D.B. FDA Public Health Advisory: Avoidance of
    serious x-ray-induced skin injuries to patients during
    fluoroscopically-guided procedures. Rockville, MD: U.S.
    Department of Health and Human Services;
    HHS(FDA)(CDRH); communication on September 30, 1994.

Carlsson, C.A. Integral absorbed doses in roentgen diagnostic procedures. ACTA Radiol. Ther. Phys., Biol. 3:310-326; 1965.

Carlsson, G.A.; Carlsson C.A. Effective energy in diagnostic radiology. A critical review. Phys. Med. Biol. 29:953-958; 1984.

Clarkson, D.McG.; Phil, M.; Brennen, S.E. Use of a microcomputer for the estimation of x-ray dose received by the fetus. Br. J. Radiol. 60:1119-1123; 1987.

Code of Federal Regulations. 21 CFR 1020.31(d)(2)(ii); April 4, 1985.

Conference of Radiation Control Program Directors. Average patient exposure/dose guides-1992. CDCPD Publication 92-4; 1992.

Federal Register. Mammography facilities - Requirements for accrediting bodies and quality standards and certification requirements; Interim rules. Federal Register Vol. 58, No. 243; December 21, 1993a.

Federal Register. Rules and regulations; 1020.31 radiographic equipment and 1020.32 fluoroscopic equipment. Federal Register Vol. 58, No. 83; May 3, 1993b.

Fife, A.J.; Wilson, D.J.; Lewis, C.A. Entrance exposure and ovarian doses in hysterosalpingography. Br. J. Radiol. 67:860-863; 1994.

Food and Drug Administration. Avoidance of serious x-ray induced skin injuries to patients during fluoroscopically-guided procedures. Rockville, MD: FDA; communication: September 9, 1994.

Gray, J.E.; Ragozzino, M.W.; Van Lysel, M.S.; Burke, T.M.
    Normalized organ doses for various diagnostic
    radiographic procedures. Am. J. Radiol. 137:463-470;
    1981.

Grosswendt, B. Backscatter factors for x-rays generated at
    voltages between 10 and 100 kV. Phys. Med. Biol.
    29:579-591; 1984.

Grosswendt, B. Dependence of the photon backscatter factor
    for water on source-to-phantom distance and irradiation
    field size. Phys. Med. Biol. 35:1233-1245; 1990.

Harrison, R.M. Central-axis depth-dose data for diagnostic
    radiology. Phys. Med. Biol. 26:657-670; 1981.

Harrison, R.M. Backscatter factors for diagnostic radiology
    (1-4 mm Al HVL). Phys. Med. Biol. 27:1465-1474; 1982.

Harrison, R.M. Tissue-air ratios and scatter-air ratios for
    diagnostic radiology (1-4 mm Al HVL). Phys. Med. Biol.
    28:1-18; 1983.

Hendee. W.R.; Medical Radiation Physics: Roentgenology,
    Nuclear Medicine and Ultrasound. 2nd ed. Chicago: Year
    Book Medical Publishers; 1984.

Institute of the Physical Sciences in Medicine. Report of
    the IPSM working party on low- and medium-energy x-ray
    dosimetry. Phys. Med. Biol. 36:1027-1038; 1991.

International Commission On Radiation Units And
    Measurements. Average energy required to produce an
    ion pair. Washington, DC: ICRU; ICRU Report 31; 1979.

International Commission On Radiation Units And
    Measurements. Radiation Quantities and Units.
    Washington, DC: ICRU; ICRU Report 33; 1980.

International Commission On Radiation Units And
    Measurements. Phantoms and computational models in
    therapy, diagnosis and protection. Bethesda, MD: ICRU;
    ICRU Report 48; 1992.

International Commission on Radiological Protection.
    Reference man: Anatomical, physiological and metabolic
    characteristics. Oxford: Pergamon Press; ICRP
    Publication 23; 1975.

International Commission on Radiological Protection. 1990
    recommendations of the International Commission on
    Radiological Protection. Oxford: Pergamon Press; ICRP
    Publication 60; 1991.

Johns, H.E.; Cunningham, J.R. The Physics of Radiology. 4th
    ed. Springfield, IL: Charles C. Thomas; 1983.

Joint Commission on Accreditation of Health Care
    Organizations. Accreditation manual for hospitals
    (1991). Chicago, IL: JCAHO; 1991.

Jones, D.G.; Wall, B.F. Organ doses from medical x-ray
    examinations calculated using Monte Carlo techniques.
    London: National Radiological Protection Board; NRPB-
    R186; 1985.

Klevenhagen, S.C. Experimentally determined backscatter
    factors for x-rays generated at voltages between 16 and
    140 kV. Phys. Med. Biol. 34:1871-1882; 1989.

Knoll, G.F. Radiation Detection and Instrumentation. New
    York: John Wiley and Sons; 1979.

Kramer, R.; Zankl, M.; Williams, G.; Drexler, G. The
    calculation of dose from external photon exposures
    using reference human phantoms and Monte Carlo methods,
    Part I: The male (ADAM) and female (EVA) adult
    mathematical phantoms. Gesellschaft für Strahlen-und
    Umweltforschung, München: GSF, Bericht S-885; 1982.

Le Heron, J.C. Estimation of effective dose to the patient
    during medical x-ray examinations from measurements of
    dose-area product. Phys. Med. Biol. 37:2117-2126;
    1992.

Marshall, N.W.; Faulkner, K. Normalized organ dose data
    measured as a function of field size for abdominal
    examinations. Phys. Med. Biol. 38:1131-1136; 1993.

Marshall, N.W.; Faulkner, K.; Busch, H.P.; Marsh, D.M.;
    Pfenning, H. A comparison of radiation dose in
    examination of the abdomen using different radiological
    imaging techniques. Br. J. Radiol. 67:478-484; 1994.

Meredith, W.J.; Massey, J.B. Fundamental Physics of
    Radiology. 3rd ed. Bristol: John Wright and Sons; 1977.

National Council on Radiation Protection and Measurements.
    Mammography: a user's guide. Bethesda, MD: NCRP; NCRP
    Report 85; 1986.

National Council on Radiation Protection and Measurements.
    Exposure of the U.S. population from diagnostic medical
    radiation: Recommendations of the National Council on
    Radiation Protection and Measurements. Bethesda, MD:
    NCRP; NCRP Report 100; 1989.

National Council on Radiation Protection and Measurements.
    Limitation of exposure to ionizing radiation. Bethesda,
    MD: NCRP; NCRP Report 116; 1993.

National Council on Radiation Protection and Measurements.
    Considerations regarding the unintended radiation
    exposure of the embryo, fetus or nursing child.
    Bethesda, MD: NCRP; NCRP Commentary 9; 1994.

Okkalides, D.; Fotakis, M. Patient effective dose resulting
    from radiographic examinations. Br. J. Radiol. 67:564-
    572; 1994.

Pentecost, M.J.; Interventional radiology perspective on the Food and Drug Administration warning on fluoroscopy. Fairfax, VA: Society of Cardiovascular and Interventional Radiography; SCVIR communication on September 30, 1994.

Radiological Health Bulletin. Training underway for NEXT fluoroscopic surveys. Rockville, MD: Center for Devices and Radiological Health; Vol. XXV, No. 2; February, 1991.

Ragozzino, M.W.; Gray, J.E.; Burke, T.M.; Van Lysel, M.S. Estimation and minimization of fetal adsorbed dose: Data from common radiographic examinations. Amer. J. Radiol. 137:667-671; 1981.

Rosenstein, M. Organ doses in diagnostic radiology. Rockville, MD: U.S. Department of Health, Education, and Welfare; HEW Publication (FDA) 76-8031; 1976.

Rosenstein, M. Handbook of selected tissue doses for projections common in diagnostic radiology. Rockville, MD: U.S. Department of Health and Human Services; HHS Publication (FDA) 89-8031; 1988.

Rosenstein, M.; Anderson, L.W.; Warner, G.G. Handbook of glandular tissue doses in mammography. Rockville, MD: U.S. Department of Health and Human Services; HHS Publication (FDA) 85-8239; 1985.

Rosenstein, M.; Suleiman, O.H.; Burkhart, R.L.; Stern, S.H.; Williams, G. Handbook of selected tissue doses for the upper gastrointestinal fluoroscopic examination. Rockville, MD: U.S. Department of Health and Human Services; HHS Publication (FDA) 92-8282; 1992.

Sax, N.I.; Lewis, R.J.Sr. Hawley's Condensed Chemical Dictionary. 11th ed.; New York: Van Nostrand Reinhold Company; 1987.

Schultz, F.W.; Geleijns, J.; Zoetelief, J. Calculation of dose conversion factors for posterior-anterior chest radiography of adults with a relatively high-energy x-ray spectrum. Br. J. Radiol. 67:775-785; 1994.

Schulz, R.J.; Gignac, C. Application of tissue-air ratios for patient dosage in diagnostic radiology. Radiology 120:687-690; 1976.

Seuntjens, T.; Thierens, H.; Van der Plaetsen, A.; Segaert, O. Conversion factor f for x-ray beam qualities specified by peak tube potential and HVL value. Phys. Med. Biol. 32:595-603; 1987.

Shrimpton, P.C.; Wall, B.F. An evaluation of the Diamentor transmission ionization chamber in indicating exposure-area product (Rcm^2) during diagnostic radiological examinations. Phys. Med. Biol. 27:871-878; 1982.

Spiers, F.W. Effective atomic number and energy absorption in tissues. Br. J. Radiol. 19:52-63; 1946.

Spokas, J.J.; Meeker, R.D. Investigation of cables for ionization chambers. Med. Phys. 7:135-140; 1980.

Sprawls. P.Jr.; <u>Physical Principles of Medical Imaging</u>. Rockville, MD: Aspen Publishers; 1987.

Storm, E.; Israel, H.I.; Photon cross sections from 1 keV to 100 MeV for elements Z=1 to Z=100. Nuclear Data Tables A7:565-681; 1970.

Stovall, M.; Blackwell, C.R.; Cundiff, J.; Novak, D.H.; Palta, J.R.; Wagner, L.K.; Webster, E.W.; Shalek, R.J. Fetal dose from radiotherapy with photon beams: Report of AAPM Radiation Therapy Committee Task Group No. 36. Med. Phys. 22:63-82; 1995.

Ter-Pogossian, M.M.; <u>The Physical Aspects of Diagnostic Radiology</u>. New York: Harper and Row; 1967.

U.S. Department of Health and Human Services. Evaluation of
    radiation exposure from diagnostic radiology
    examinations: General recommendations. Rockville, MD:
    USDHHS; HHS Publication (FDA) 85-8246; 1985.

U.S. Department of Health, Education, and Welfare.
    Radiological Health Handbook revised edition.
    Rockville, MD: FDA; 1970.

University of Wisconsin - Accredited Dosimetry Calibration
    Laboratory. Description of reported UW-ADCL calibration
    factors. Madison, WI: UW-ADCL; 1993.

Waggener, R.G.; Kereiakes, J.G.; Shalek, R.J. editors;
    Handbook of Medical Physics. 2nd printing. Boca Raton,
    FL: CRC Press; 1985.

Wagner, L.K.; Elfel, P.J.; Geise, R.A. Potential biological
    effects following high x-ray dose interventional
    procedures. J. Vas. Int. Radiol. 5:71-84; 1994.

Wagner, L.K.; Lester, R.G.; Saldana, L.R. Exposure of the
    Pregnant Patient to Diagnostic Radiation. Philadelphia,
    PA: J.B. Lippincott; 1985.

Wall, B.F.; Harrison, R.M.; Spiers, F.W. Patient dosimetry
    techniques in diagnostic radiology. York, England:
    Institute of Physical Science in Medicine; IPSM Report
    53; 1988.

Weber, J.; van den Berge, D.J. The effective atomic number
    and the calculation of the composition of phantom
    materials. Br. J. Radiol. 42:378-383; 1969.

White, D.R. An analysis of the z-dependence of photon and
    electron interactions. Phys. Med. Biol. 22:219-228;
    1977a.

White, D.R. The formulation of tissue substitute materials
    using basic interaction data. Phys. Med. Biol. 22:889-
    899; 1977b.

White, D.R. Tissue substitutes in experimental radiation physics. Med. Phys. 5:467-479; 1978.

BIOGRAPHICAL SKETCH

I was born in a small city located in the state of New York during the year of 1955. My family resided near that small city until the year of 1965, whereupon my family relocated to the capital city of the state of North Carolina. While residing in New York and North Carolina, I attended public school. My undergraduate education was received at North Carolina State University and ended with receipt of a Bachelor of Science degree in zoology and a Bachelor of Arts degree in chemistry.

My graduate education began at the University of North Carolina at Chapel Hill, where I received a Master of Science degree in radiological hygiene. I am ending my graduate education at the University of Florida, where I will receive a Doctor of Philosophy degree in medical physics. During my graduate studies at the University of Florida, I was wedded and became a proud parent of a stepdaughter and a daughter.

I certify that I have read this study and that in my opinion it conforms to acceptable standards of scholarly presentation and is fully adequate, in scope and quality, as a dissertation for the degree of Doctor of Philosophy.

Walter Mauderli, Chairman
Professor Emeritus of Nuclear
    Engineering Sciences

I certify that I have read this study and that in my opinion it conforms to acceptable standards of scholarly presentation and is fully adequate, in scope and quality, as a dissertation for the degree of Doctor of Philosophy.

Lawrence T. Fitzgerald, Cochairman
Associate Professor of Nuclear
    Engineering Sciences

I certify that I have read this study and that in my opinion it conforms to acceptable standards of scholarly presentation and is fully adequate, in scope and quality, as a dissertation for the degree of Doctor of Philosophy.

G. Ronald Dalton
Professor of Nuclear Engineering
    Sciences

I certify that I have read this study and that in my opinion it conforms to acceptable standards of scholarly presentation and is fully adequate, in scope and quality, as a dissertation for the degree of Doctor of Philosophy.

William S. Properzio
Professor of Environmental
    Engineering Sciences

I certify that I have read this study and that in my opinion it conforms to acceptable standards of scholarly presentation and is fully adequate, in scope and quality, as a dissertation for the degree of Doctor of Philosophy.

W. Emmett Bolch, Jr.
Professor of Environmental
    Engineering Sciences

This dissertation was submitted to the Graduate Faculty of the College of Engineering and to the Graduate School and was accepted as partial fulfillment of the requirements for the degree of Doctor of Philosophy.

May 1996

Winfred M. Phillips
Dean, College of Engineering

Karen A. Holbrook
Dean, Graduate School